

1 **Observations suggest that North African dust absorbs less solar radiation than**
2 **models estimate.**

3
4 Adeyemi A. Adebiyi^{1,*}, Yue Huang^{2,3,4}, Bjørn H. Samset⁵ and Jasper F. Kok²

5 ¹Department of Life and Environmental Sciences, University of California - Merced,
6 Merced, CA, USA

7 ²Department of Atmospheric and Oceanic Sciences, University of California-Los
8 Angeles, Los Angeles, CA, USA

9 ³NASA Goddard Institute for Space Studies, New York, NY 10025, USA

10 ⁴Earth Institute, Columbia University, New York, NY 10025, USA

11 ⁵CICERO Center for International Climate Research, Oslo, Norway

12
13 **Corresponding author:* Adeyemi Adebiyi; Email: aaadebiyi@ucmerced.edu;
14 Department of Life and Environmental Sciences, University of California-Merced, 5200
15 North Lake Road, Merced, CA 95343.
16

17 **Abstract**

18 Desert dust accounts for a large fraction of shortwave radiation absorbed by aerosols,
19 which adds to the climate warming produced by greenhouse gases. However, it remains
20 uncertain exactly how much shortwave radiation dust absorbs. Here, we leverage in-situ
21 measurements of dust single-scattering albedo to constrain absorption at mid-visible
22 wavelength by North African dust, which accounts for approximately half of global dust.
23 We find that climate and chemical transport models overestimate North African dust
24 absorption aerosol optical depth (AAOD) by up to a factor of two. This occurs primarily
25 because models overestimate the dust imaginary refractive index, the effect of which is
26 partially masked by an underestimation of large dust particles. Similar factors might
27 contribute to an overestimation of AAOD retrieved by the Aerosol Robotic Network,
28 which is commonly used to evaluate models. The overestimation of dust absorption by
29 models could lead to substantial biases in simulated dust impacts on the Earth system,
30 including warm biases in dust radiative effects.

31

32

33 **Introduction**

34 Most of the aerosol species in the atmosphere produce a cooling effect that opposes the
35 warming effect produced by greenhouse gases¹. However, mineral dust is one of the three
36 main aerosol species, in addition to black carbon and brown carbon, that absorb solar
37 radiation and therefore could add to the warming produced by greenhouse gases^{1,2}. The
38 exact amount of solar radiation that dust absorbs greatly affects its impact on the global
39 climate system. For instance, whether the net direct radiative effect of dust aerosols
40 warms or cools the global climate system depends, in large part, on the amount of solar
41 radiation absorbed by dust^{3–5}. Therefore, determining the extent of dust absorption of
42 solar radiation is critical to determining whether future changes in atmospheric dust will
43 slow or accelerate the projected warming of the climate system by greenhouse gases⁶.
44 Beyond its direct radiative impacts, dust shortwave absorption also modifies atmospheric
45 temperature profiles, thereby altering atmospheric circulations, cloud distributions, and
46 precipitation^{7–9}. For example, enhanced dust shortwave absorption within the Saharan air
47 layer can reduce the intensification of tropical cyclones over the North Atlantic Ocean by
48 enhancing the low-level temperature inversion and increasing the vertical wind shear,
49 which could ultimately weaken associated precipitation^{10,11}.

50

51 Despite the importance of dust shortwave absorption on weather and the climate
52 system¹², the exact amount of shortwave radiation absorbed by dust in the atmosphere
53 remains highly uncertain^{13,14}. This uncertainty in estimating dust shortwave absorption is
54 partially due to uncertainties in the microphysical properties of dust used in climate and
55 chemical transport models (Figure 1)^{12,15}. The amount of shortwave radiation absorbed by
56 dust aerosols is quantified by the dust absorption aerosol optical depth (dust AAOD) – a
57 parameter that depends on dust extinction, quantified by the dust aerosol optical depth
58 (AOD), and the fraction of that extinction that is due to absorption, quantified by the
59 single scattering albedo (SSA; Figure 1). Whereas global dust extinction scales with
60 overall dust mass loading and has been effectively constrained using remote sensing
61 observations^{16–18}, estimates of dust SSA remain very uncertain^{12,15}. This is because dust
62 SSA primarily depends on the dust size distribution, dust shape, and the dust
63 mineralogical composition (characterized by dust refractive index), and all these
64 microphysical properties are poorly constrained in climate and chemical transport models
65 (Figure 1). For example, recent studies have shown that dust size distributions assumed in
66 global aerosol models overestimate the amount of fine dust particles (with diameter, $D \leq$
67 5 μm) and greatly underestimate the amount of large or coarse dust particles ($D \geq 5 \mu\text{m}$)
68 in the atmosphere compared to *in-situ* measurements^{3,19–21}. Since coarse dust absorbs
69 more shortwave radiation than fine dust^{22,23}, this underestimation of coarse dust particles
70 could bias estimates of dust AAOD in climate and chemical transport models^{5,20,24}.
71 Furthermore, a coarse irregularly-shaped dust particle absorbs more radiation than a
72 spherical dust particle of the same volume and mineralogy, causing errors in models
73 because of the common assumption that dust is spherical^{25–27}. Another factor contributing
74 to large uncertainties in the dust SSA is that it primarily depends on iron-bearing
75 minerals, mainly hematite and goethite^{28–31}. These minerals have substantial but poorly
76 known spatial variabilities, differing significantly between different dust sources^{32,33}.
77 However, most climate and chemical transport models still implicitly assume an invariant

78 mineralogical composition by using constant dust refractive index values that do not vary
79 in space and time^{34,35}. Because dust aerosols contribute more than a third of the total
80 shortwave absorption in most climate and chemical transport models¹⁴, therefore, large
81 uncertainties in dust AAOD could substantially influence the overall impacts of aerosol
82 absorption in the atmosphere.

83
84 One reason for the large uncertainties in dust shortwave absorption and the associated
85 dust size distribution and refractive index is that these dust properties are difficult to
86 obtain from remote-sensing observations. Because the instruments on these remote-
87 sensing platforms cannot directly measure aerosol size distributions and refractive
88 indices, inversion algorithms are needed to retrieve these key aerosol properties.
89 However, these inversion algorithms are, in turn, generally underdetermined and thus
90 require important underlying assumptions, such as the representation of dust shape^{36,37},
91 which could lead to substantial uncertainties in the retrieved absorption aerosol
92 properties³⁸. One such remote-sensing retrieval from the ground-based AErosol RObotic
93 NETwork (AERONET) is widely used to characterize atmospheric aerosol properties and
94 evaluate climate and chemical transport models³⁹. However, previous studies have
95 highlighted that AERONET retrievals of dust size distribution may be too fine when
96 compared against near-coincident aircraft-based *in-situ* measurements over North
97 Africa, although these measurements are not column-integrated and thus not directly
98 comparable^{40,41}. In addition, comparisons between AERONET retrievals of refractive
99 index and mineralogical analysis of dust particles measured onboard an aircraft indicated
100 substantial differences in the estimated dust imaginary refractive index^{42,43}. Therefore,
101 uncertainties in dust size distribution and dust refractive index in both remote-sensing
102 retrievals and model simulations have made it difficult to estimate dust shortwave
103 absorption accurately and have introduced substantial uncertainties in estimates of dust
104 impacts on regional and global climate systems^{3,7,12,44,45}.

105
106 Here we address these problems by leveraging observationally based constraints on size-
107 resolved dust properties and dust refractive index to constrain the dust shortwave
108 absorption (Figure 1). Specifically, we developed a framework that leveraged dozens of
109 *in-situ* measurements of dust SSA to constrain the dust refractive index, which is
110 combined with observationally based constraints on size-resolved dust properties to
111 constrain the dust AAOD at mid-visible (550 nm) wavelength (Methods & fig. S-1).
112 Although dust shortwave absorption occurs across the solar spectrum, we focus on the
113 550 nm wavelength and use it as a representative wavelength. This is because, 550 nm
114 wavelength is the reference wavelength used in most modeling and remote sensing
115 studies^{16,46}. Estimates of dust shortwave absorption at other visible wavelengths can be
116 obtained by combining measurements of the spectral distribution of dust absorption
117 properties^{47,48} with our constraints at 550 nm wavelength. In addition, we focus on dust
118 emitted from North Africa, the world's largest dust source, because it accounts for more
119 than half of the global dust mass burden^{49,50}. As such, uncertainties in the absorption
120 properties of North African dust can substantially influence estimates of dust impacts on
121 the global climate system⁵¹. Overall, our observationally based constraints suggest that
122 North African dust absorbs substantially less shortwave radiation than estimated by an
123 ensemble of climate and chemical transport model simulations and retrieved by the

124 AERONET inversion algorithms. This suggests that models and retrievals overestimate
125 dust shortwave absorption, implying substantial biases in estimates of dust impacts on the
126 energy balance, precipitation, and other critical aspects of the regional and global climate
127 systems.

128

129 **Results and Discussion**

130 **The imaginary refractive index of North African dust**

131 We obtained constraints on the imaginary refractive index of North African dust by
132 leveraging more than a dozen *in-situ* measurements of dust single scattering albedo
133 (SSA) over North Africa (Figure 1 & fig. S-1). Specifically, we used an optimization
134 method⁵², whereby we obtained the dust imaginary refractive index at 550 nm
135 wavelength that yields a dust SSA in optimal agreement with the collection of *in-situ*
136 SSA measurements (see cyan-filled bars and circles in Figure 2a & b, respectively, and
137 more details in Table S-1). Our estimates of dust SSA better reproduce the compilation of
138 *in-situ* measurements of dust SSA over North Africa than estimates from climate and
139 chemical transport models (Figure 2a). Specifically, the climate and chemical transport
140 models consistently underestimate the dust SSA *in-situ* measurements at 550 nm
141 wavelength. To put these measurements and model simulations of dust SSA on a similar
142 footing, we calculated the simulated values over the same diameter range, height range,
143 locations, and season as reported for the measurements (see Methods). We made the
144 comparison of dust SSA for two sets of model simulations – an ensemble of six selected
145 models (gray bars in Figure 2a) and an ensemble of eight models that are part of the
146 AeroCom (Aerosol Comparison between Observations and Models) Phase III project
147 (dark-green bars in Figure 2a) (see Table S-2 for details of both sets of models). We
148 estimated mean dust SSA values of about 0.95 (standard error: 0.94 - 0.97) and 0.94
149 (standard error: 0.93 - 0.96) for the ensemble of selected models and AeroCom models,
150 respectively. In contrast, the *in-situ* measurements revealed that North African dust
151 generally has higher dust SSA values with a mean of about 0.97 (mean values range
152 between 0.92 and 0.99) than the climate model simulations, over the same diameter
153 range, height range, locations, and season. These discrepancies between the *in-situ*
154 measurements and simulated dust SSA are consistent for cases with sub-micron diameter
155 cut-off^{23,41,53-56} and for cases that account for larger dust particles⁵⁷⁻⁵⁹. Overall, the
156 underestimation of dust SSA in the ensemble of selected models and AeroCom models
157 can result in a mean bias of approximately -5% over some locations and collectively
158 result in root-mean-square errors of up to a factor of two larger than our estimate of dust
159 SSA (fig. S-2).

160

161 Consequently, we find the imaginary refractive index that optimally reproduces the
162 compilation of the *in-situ* SSA measurements of North African dust is much smaller than
163 assumed in most climate and chemical transport models (Figure 2c). Specifically, North
164 African dust has a mean imaginary refractive index at 550 nm wavelength of 0.0012 (one
165 standard error range of 0.0009 - 0.0016; pink/red bars in Figure 2c). Our analysis focused
166 on constraining the dust imaginary refractive index because dust shortwave absorption
167 depends more sensitively on the imaginary part of the refractive index than on its real
168 part (e.g., fig. S-3)^{15,31,60,61}. In addition, although our source-resolved constraints on dust
169 imaginary refractive index are informed by a compilation of *in-situ* dust SSA

170 measurements, they are consistent with previous lab-based measurements of imaginary
171 refractive index from mineral soil dust^{29,62,63}. For example, Di Biagio et al.²⁹ used parent
172 soil samples from North Africa and found that the dust imaginary refractive index over
173 the Sahel has a relatively larger uncertainty than the Sahara dust source region (see blue
174 bars in Figure 2c for interpolated values at 550 nm wavelength). In contrast, most climate
175 model simulations ignore these regional differences in dust imaginary refractive index
176 and assume that the refractive indices are invariant in space and time³⁴. The average dust
177 imaginary refractive index for the ensemble of selected and AeroCom models are
178 respectively 0.0029 (standard error: 0.0014 - 0.0030) and 0.0026 (0.0011 - 0.0031) (see
179 Table S-2). Therefore, on average, these climate and chemical transport models
180 overestimate the imaginary refractive index of North African dust by more than a factor
181 of two.

182
183 Consistent with these estimates in climate and chemical transport models, we also find
184 that dust-dominated AERONET retrievals estimate a larger imaginary refractive index at
185 550 nm wavelength over North Africa than obtained from our observationally based
186 constraints (compare pink/red and purple bars in Figure 2c). Since AERONET retrievals
187 account for both dust and non-dust aerosol species (such as smoke aerosols), we obtained
188 dust-dominated AERONET retrievals by applying strong criteria, including using an
189 Ångström exponent of less than 0.2 to discriminate the observations that predominantly
190 contain dust aerosols from observations containing other aerosol species⁴⁷ and thereby
191 minimizing the non-dust component in the resulting estimates (see Methods). In addition,
192 to put the AERONET retrievals on a similar footing as our constraints and ensemble of
193 model simulations and because of the non-linear dependence of complex refractive index
194 on wavelength, we fit a second-order polynomial as a function of wavelength between
195 440 and 1020 nm to obtain interpolated values of AERONET-retrieved imaginary
196 refractive at 550 nm wavelength⁶³⁻⁶⁵. We find that the dust-dominated AERONET-
197 retrieved imaginary refractive index is approximately 0.0019 (0.0016 - 0.0021) for all of
198 North Africa. Although the AERONET-retrieved imaginary refractive index is slightly
199 less than the ensemble mean dust imaginary refractive index used in models, it is
200 comparable to values used in some members of the selected and AeroCom models (see
201 Figure 2c and Table S-2). In addition, like most climate models, AERONET-retrieved
202 imaginary refractive index is larger than our constraints on dust imaginary refractive
203 index over North Africa by about 54%.

204
205 **The shortwave absorption aerosol optical depth of North African dust**
206 We find that climate models and AERONET retrievals estimate substantially more
207 absorption of shortwave radiation by North African dust aerosols than indicated by our
208 observationally based constraints. We obtained our constraints on the dust absorption
209 aerosol optical depth (dust AAOD) at 550 nm wavelength by combining our constraints
210 on source-resolved dust imaginary refractive index (Figure 2c) with observationally
211 informed constraints on dust shape²⁷, column-integrated dust size distribution, and dust
212 mass loading^{3,21} (see Methods). As a result, we find that the dust AAOD averaged over
213 the North African continent is about 0.0094 (0.0073-0.0120) (Figure 3a). However, the
214 simulated dust AAOD values over the same area are approximately 0.0110 (0.0064-
215 0.0494) and 0.0180 (0.0148-0.0219) for the ensemble of selected and AeroCom models,

216 respectively (Figure 3b & c). Furthermore, averaging over both the continent and the
217 ocean, where North African dust sources dominate global dust loading (by more than 80
218 %; see the dashed black contour in Figure 3a-c)⁵⁰, our constraint on dust AAOD is about
219 0.0045 (0.0035-0.0057), whereas the simulated dust AAOD values are 0.0053 (0.0030-
220 0.0232) and 0.0090 (0.0059-0.0107) for the ensemble of selected and AeroCom models,
221 respectively. Therefore, relative to our constraints, climate and chemical transport models
222 overestimate the shortwave aerosol absorption by up to a factor of two in regions where
223 North African dust dominates.

224
225 Similarly, we also find that dust-dominated AERONET retrievals estimate substantially
226 greater shortwave absorption over North Africa than indicated by our observationally
227 based constraints (Figure 3f). As highlighted above, we use a second-order fit to
228 interpolate to 550 nm wavelength⁶³⁻⁶⁵ and also applied strong criteria to discriminate the
229 AERONET retrievals that are predominantly dust aerosols and thus minimize the non-
230 dust component in the AERONET-retrieved total AAOD (see Methods). To put the
231 AERONET retrievals, climate model simulations, and our constraints on a similar
232 footing, we obtained the column-integrated non-dust AAOD from the ensemble of
233 AeroCom models and added it to our constraints on column-integrated dust AAOD. Over
234 each AERONET station (cf. Figure 2b), the dust-dominated retrievals are consistently
235 larger than the total AAOD of our estimate. This possible overestimation of AAOD could
236 reach up to a factor of three over some AERONET stations (fig. S-4). In addition, the
237 difference between AERONET-retrieved total AAOD and our estimates for Saharan
238 stations is about 55% more than that for Sahelian stations (Figure 3f). Collectively over
239 North Africa, the average dust-dominated AERONET-retrieved total AAOD is 0.029
240 (0.021 - 0.031), whereas our estimate over the same locations is 0.017 (0.010 - 0.027;
241 Figure 3f). Although AERONET thus estimates a larger total AAOD than our constraints,
242 the retrieved value is comparable with model-estimated column-integrated total AAOD,
243 which is similarly collocated with the dust-dominated North African AERONET stations
244 (Figure 3f). Overall, our analysis suggests that North African dust might absorb less
245 shortwave radiation than simulated in climate and chemical transport models or obtained
246 from dust-dominated AERONET retrievals.

247
248 **The cause of possible biases in the simulated and retrieved North African dust**
249 **shortwave absorption.**

250 Our observationally based constraints thus show a substantially lower shortwave
251 absorption by dust than simulated by climate models and retrieved by AERONET.
252 Although we cannot rule out that this difference is due to biases in the *in situ*
253 measurements of the single-scattering albedo used in our analysis, these results suggest
254 that models and AERONET retrievals might overestimate dust shortwave absorption. To
255 understand the cause of this possible overestimation, we decomposed the bias in dust
256 AAOD by examining the contribution of the input parameters. Specifically, we assessed
257 the contribution to the overall bias in the ensemble of selected models due to the bias in
258 the simulated dust refractive index and the size-resolved dust properties, which include
259 the dust load, dust shape, and dust size distribution (see Methods).

260

261 We find that the bias in the simulated dust AAOD is a strong function of dust diameter
262 (Figure 4a). Averaged over the region where North African dust sources dominate global
263 dust loading (by more than 80 %; see dashed contour in Figure 3)⁵⁰, the ensemble of
264 selected models overestimates dust AAOD for fine dust particles ($D \leq 5\mu\text{m}$) by 0.0021
265 (-0.0003 to +0.0044) but underestimates it for coarse dust particles by -0.0013 (-0.0016 to
266 -0.0009). This contrast between the overestimation of dust AAOD for fine dust and the
267 underestimation of dust AAOD for coarse dust is primarily driven by the inherent bias in
268 the simulated size-resolved dust mass loading. Specifically, climate and chemical
269 transport models overestimate the fraction of fine dust particles and underestimate the
270 fraction of coarse dust particles compared to *in-situ* measurements over North Africa
271 (Figure 4b). Depending on the model, the underestimation of coarse dust can be up to
272 approximately one-and-a-half orders of magnitude (colored lines Figure 4b). In contrast,
273 DustCOMM (Dust Constraints from joint Observational-Modelling experiMental
274 analysis), the observationally constrained dust size distribution used in this study,
275 captures the measurements better than the climate model simulations (compare red lines
276 with other lines in Figure 4b).

277
278 In addition, and across the diameter range, we also find that the bias in dust imaginary
279 refractive index contributes a substantial fraction of the bias in the simulated dust AAOD
280 (Figure 4a). Specifically, the overestimation of dust imaginary refractive index in the
281 ensemble of selected models (Figure 2c) is primarily responsible for the overestimation
282 of all North African dust AAOD (green bars in Figure 4a). This contribution of the bias
283 in dust imaginary refractive index to the bias in the dust AAOD is masked by the
284 contribution of the bias in size-resolved dust properties, which include the size-resolved
285 dust mass load and the shape representation. That is, the model overestimation of the fine
286 dust load results in an overestimation of dust AAOD; the model underestimation of the
287 coarse dust load results in an underestimation of dust AAOD; and the spherical
288 representation of dust shape results in an underestimation of dust AAOD. Whereas the
289 resulting collective bias in the size-resolved dust properties results in an underestimation
290 of the simulated North-African dust AAOD by -0.0013 (-0.0032 to +0.0054; cyan bar in
291 Figure 4a third column), the bias in the dust imaginary refractive index alone adds an
292 overestimation of 0.0023 (0.0006 – 0.0041). Put together, the bias in the representation of
293 simulated dust refractive index and size-resolved dust properties dust explains the
294 majority (> 70%) of the total discrepancy in the simulated dust AAOD for the ensemble
295 of selected climate models (compare the orange and grey bars in Figure 4a). Overall, our
296 analysis indicates that approximately half of the model overestimation of the simulated
297 dust AAOD due to the overestimation of the dust imaginary refractive index is offset by
298 the model underestimation of coarse dust.

299
300 As with the ensemble of selected global aerosol models, we find that the AERONET-
301 retrieved aerosol size distribution and imaginary refractive index explain the difference in
302 total AAOD between dust-dominated AERONET retrievals and our estimates.
303 Specifically, the AERONET-retrieved aerosol size distribution over dust-dominated
304 locations overestimates fine particles ($D \leq 5\mu\text{m}$) and underestimates coarse particles
305 ($D \geq 5\mu\text{m}$) by about the same amount as the dust size distribution in the ensemble of
306 selected models (compare purple line with other lines in Figure 4c). Similarly, as shown

307 above (Figure 2c), the AERONET-retrieved imaginary refractive index overestimates our
308 constraints on the dust imaginary refractive index by a similar amount as the ensemble of
309 selected and AeroCom models. These contributions from the mean aerosol size
310 distribution and imaginary refractive index to the overestimation of retrieved AAOD are
311 similar regardless of the Ångström exponent used to discriminate dust-dominated
312 measurements over North Africa (fig. S-5). This suggests that the overestimation in dust-
313 dominated AERONET-retrieved AAOD and its associated uncertainties in the retrieved
314 aerosol imaginary refractive index and aerosol size distribution are primarily due to the
315 uncertainties in retrievals during dusty conditions, and for instance not due to
316 contamination by other aerosol species. Overall, our results suggest that the possible
317 overestimation of retrieved and simulated North African dust shortwave absorption is
318 driven primarily by biases in dust size distribution and dust imaginary refractive index
319 (Figure 4).

320

321 **Implications of the bias in the simulated and retrieved North African dust 322 shortwave absorption.**

323 Our finding that climate model simulations and dust-dominated AERONET retrievals
324 might overestimate dust shortwave absorption has important implications for dust
325 impacts on the regional and global climate system. This is because North African dust
326 sources emit more than half of the world's dust aerosols^{49,50} and because inaccurate
327 representations of dust absorption properties would have important consequences for our
328 understanding of dust impacts on the global climate system⁵¹. One such consequence is
329 that the bias in simulated and retrieved dust shortwave absorption could affect the
330 estimates of regional dust direct radiative effects (DRE) with potential impacts on the
331 global energy balance. For example, an overestimated shortwave dust imaginary
332 refractive index (e.g., Figure 2c) could result in a warm bias for the shortwave DRE^{5,13}.
333 However, such a bias could be masked by the contemporaneous bias in the dust size
334 distribution (Figure 4) since an underestimation of coarse dust by itself produces a cold
335 bias in the shortwave DRE³. Additionally, an underestimation of coarse dust could also
336 introduce a cold bias in the longwave DRE^{3,66}, contributing to the overall bias in previous
337 modeling studies that showed that dust cools the climate system^{67–70}. Therefore, because
338 of the sensitivity of the DRE to dust absorption properties^{67,71}, an accurate representation
339 of these properties is crucial to determine whether dust warms or cools the global climate
340 system.

341

342 Furthermore, our findings also have important consequences for our understanding of
343 dust impacts on the hydrological cycle and biogeochemistry. Specifically, because dust
344 shortwave absorption induces thermodynamical and dynamical responses in the
345 atmosphere, overestimation of simulated dust AAOD could bias the temperature,
346 moisture, and wind distribution that could, in turn, affect the distributions of clouds and
347 precipitation^{7,8,44,72}. Such effects on clouds and precipitation would depend on the vertical
348 distribution of dust absorption properties, the ratio of fine and coarse dust particles, and
349 the relative position of the dust and cloud layers, which climate models have found
350 difficult to simulate accurately^{24,73}. In addition, the bias in dust absorption properties
351 could have implications for the iron mass concentration upon its deposition in the North
352 Atlantic Ocean. Specifically, because iron-oxides are the primary mineral that controls

353 the dust imaginary refractive index in the shortwave spectrum^{29,31}, our finding that
354 models overestimate dust imaginary index of refraction implies that models likely
355 overestimate the iron content in deposited dust particles. This inference is supported by
356 recent studies that indicated that surface-level total iron mass concentration is
357 overestimated near North African dust sources^{74–76}, suggesting that the fractional
358 contribution of iron-oxides to total iron mass concentration is also overestimated⁶⁷.
359 Considering this sensitivity of the radiation budget, cloud cover, precipitation
360 distribution, and biogeochemistry to dust absorption properties, the impacts of biases in
361 simulated dust AAOD on the regional and global climate system could be substantial.
362

363 In addition to the consequences of the overestimation of dust absorption in climate
364 models, our findings also have implications for retrievals of aerosol absorption properties
365 from remotely sensed observations, particularly near dust source regions such as North
366 Africa. Specifically, our results indicate that AERONET retrievals at dust-dominated
367 locations might overestimate the imaginary refractive index and underestimate the
368 contribution of coarse aerosols. Such uncertainties in aerosol properties could be
369 propagated into other applications within remote-sensing and modeling communities that
370 utilize AERONET datasets as a benchmark. For example, most satellite-based remote-
371 sensing retrievals rely on algorithms that often leverage AERONET retrievals of aerosol
372 size distribution and refractive index to discriminate different aerosol types in the
373 atmosphere⁷⁷. One such satellite-based retrieval is from CALIPSO (Cloud-Aerosol Lidar
374 and Infrared Pathfinder Satellite Observations), where previous studies have attributed
375 the possible underestimation of its extinction coefficients to a bias in the dust lidar ratio,
376 which in turn has been estimated based on AERONET retrievals of aerosol size
377 distribution and complex refractive index^{78,79}. In addition, AERONET retrievals are
378 generally used as a benchmark with which model simulations of aerosol properties are
379 constrained and validated⁶⁷. For example, Bond et al.⁸⁰ adjusted the simulated direct
380 radiative forcing of black carbon because climate models substantially underestimated
381 AAOD when compared against AERONET retrievals (see also Figure 3f). However,
382 given that our results suggest that AERONET-retrieved dust-dominated AAOD might be
383 overestimated over North Africa, such adjustments of the simulated radiative forcing
384 could result in an overestimation of aerosol direct radiative forcing. Therefore, because of
385 the global coverage of the AERONET stations, a more accurate constraint on the
386 AERONET-retrieved aerosol size distribution and refractive index is crucial for the
387 retrieval of aerosol properties from other remote-sensing platforms and to better constrain
388 model simulations of the impacts of dust and other absorbing aerosols on key aspects of
389 the Earth system.

390

391 Since our findings rely on *in-situ* dust SSA measurements and other input observational-
392 based parameters over North Africa, it is subject to some important limitations (see
393 Methods for details). One of these limitations includes uncertainties and biases associated
394 with instrumentations, which may result in the dust SSA measurements not fully
395 accounting for all the particle sizes observed over North Africa. For example, coarse and
396 super-coarse dust particles, while present over North Africa^{3,81}, are often not measured by
397 commonly-used instruments, such as nephelometers and Particle Soot Absorption
398 Photometers^{53,82–84}. In addition, the fine-mode size range of most of the SSA

399 measurements is also susceptible to contamination by other aerosol species, such as black
400 carbon, even though these measurements are obtained over dust-dominated regions^{85,86}.
401 Additional limitations to our results may be introduced through inherent uncertainties in
402 other observationally based datasets we used as inputs, including uncertainties in the
403 DustCOMM dust size distribution, dust loading, dust shape, and the fractional
404 contribution of each dust source used to constrain the dust absorption properties (see
405 Methods). For example, uncertainties may be introduced through the assumption of a
406 representative location and height range used for dust SSA measurements (Figure 2a), as
407 well as the exclusion of particles larger than $D \geq 20 \mu\text{m}$ in the DustCOMM dust size
408 distribution. We propagate some of these uncertainties into our estimates of dust
409 refractive index and dust AAOD by using a non-parametric procedure based on the
410 bootstrap method^{87,88} that randomly selects (with replacement) from the probability
411 distributions of each of the input parameters (see Methods).

412
413 Because of these limitations and uncertainties, our calculated errors on dust imaginary
414 refractive index and dust AAOD should be considered as lower bounds. This is
415 particularly relevant for the assessment of AERONET-derived imaginary refractive index
416 and total AAOD^{89–91}. For example, *in-situ* dust SSA measurements used to constrain
417 source-resolved dust imaginary refractive index are not directly collocated with
418 AERONET dust-dominated sites, and even in locations that are collocated, *in-situ*
419 measurements are obtained over specific atmospheric layers, whereas AERONET
420 retrievals are over the entire atmospheric column. Similarly, our comparison with
421 AERONET-retrieved total AAOD uses our constraints on dust AAOD and estimates of
422 non-dust AAOD from an ensemble of AeroCom models. However, most models
423 underestimate the burden of black carbon in the atmosphere, which dominates non-dust
424 AAOD⁸⁰. As such, the differences between our constraints and AERONET retrievals are
425 likely smaller than indicated for dust imaginary refractive index in Figure 2c and total
426 AAOD in Figure 4f. Furthermore, this suggests that the analysis cannot directly establish
427 that our constraints are more accurate than those obtained from AERONET and that the
428 overestimation of AERONET-retrieved imaginary index and AAOD are likely smaller
429 over North Africa (e.g., fig. S-5).

430
431 In conclusion, our results suggest that climate models overestimate mid-visible
432 absorption by North African dust. Specifically, we found that the imaginary refractive
433 index that optimally reproduces a compilation of *in-situ* measurements of the single-
434 scattering albedo of North African dust is less than what is assumed in most climate and
435 chemical transport models over North Africa. By itself, this underestimation of the
436 imaginary refractive index relative to what is indicated by measurements would result in
437 an overestimation of mid-visible absorption and AAOD by climate models. However, our
438 results further suggest that this overestimation might be partially mitigated by climate
439 models underestimating the abundance of coarse dust (dust diameter, $D \geq 5 \mu\text{m}$) relative
440 to *in situ* measurements. In addition, our results also suggest that similar factors may
441 contribute to an overestimation of dust-dominated total AAOD retrieved by AERONET
442 over the Sahara and Sahel regions of North Africa. Because approximately half of the
443 global dust is emitted from North African sources^{49,50}, our finding that models and remote
444 sensing retrievals might overestimate mid-visible absorption suggests potentially

445 substantial biases in estimates of dust impacts on the energy balance, precipitation,
446 biogeochemistry, and other critical aspects of the Earth system.
447

448 **Methods**

449 We constrained the spatially varying absorption optical depth (AAOD) of North African
450 dust by combining constraints on the distribution of dust mass loading and dust mass
451 absorption efficiency at 550 nm, both as a function of dust diameter (fig. S-1). The size-
452 resolved dust mass absorption efficiency and dust mass loading, in turn, depend primarily
453 on (a) the dust size distribution, (b) dust mass loading, (c) dust shape, and (d) dust
454 complex refractive index (Figure 1). We thus obtained constraints on the dust AAOD by
455 obtaining observationally informed constraints on these four key dust properties. In the
456 next few paragraphs, we summarize the methodology and datasets used to constrain these
457 dust properties and, therefore, the dust AAOD and then provide more detail for each step
458 in the following sub-sections.
459

460 To obtain constraints on the key dust properties needed to estimate dust AAOD, our
461 framework leveraged *in-situ* measurements of airborne dust particles over North Africa
462 (fig. S-1). For the first two key dust properties – the dust size distribution and dust mass
463 loading – we used the data from DustCOMM (Dust Constraints from joint Observational-
464 Modelling experiMental analysis). This dataset combined aircraft-based *in-situ*
465 measurements of dust size distribution with satellite-based and reanalysis-derived dust
466 properties and an ensemble of climate model simulations^{3,21}. Because these constraints on
467 the dust size distribution and dust mass loading rely on *in-situ* measurements, they
468 account for the coarse dust (diameter, $D \geq 5\mu\text{m}$) missing from most climate model
469 simulations³. In addition, the constraint on the third dust property – dust shape –
470 leverages the measurements compilation of dust aspect ratio and height-to-width ratio
471 from Huang et al.²⁷ to account for the asphericity of dust that is commonly neglected in
472 climate model simulations³⁴. For constraint on the last dust property – the dust refractive
473 index – we leveraged more than a dozen *in-situ* measurements of dust single scattering
474 albedo (SSA) taken over North Africa (Figure 2a). Specifically, we obtained constraints
475 on the dust imaginary refractive index by minimizing the disagreement between the
476 compilation of *in-situ* SSA measurements and our estimates of dust SSA. Our SSA
477 estimates utilized the regionally invariant constraints on dust shape and DustCOMM
478 constraints on dust size distribution obtained over the same location, altitude range,
479 season, and dust diameter range as the *in-situ* SSA measurements. With these constraints
480 on the dust size distribution, dust mass loading, dust shape, and dust refractive index, we
481 obtained constraints on dust AAOD (fig. S-1).
482

483 Furthermore, because the dust size distribution, dust mass loading, and dust refractive
484 index depend on dust source regions, we accounted for the contribution of North African
485 dust sources in the constraints on dust AAOD. Specifically, we divided North Africa into
486 two major dust source regions – the Sahara and Sahel regions (Figure 2b)^{49,50,92}.
487 Consequently, we used the observationally informed dataset obtained by Kok et al.⁹³ as
488 part of DustCOMM to constrain the fractional contribution of each source region to the
489 dust size distribution over every location. This constraint on source-resolved dust size

490 distribution is used in our constraints on size-resolved dust mass loading, dust refractive
491 index, and subsequently on dust AAOD.

492
493 One major strength of our constraints on dust AAOD is quantifying the associated
494 uncertainties for each step of the analysis. Specifically, we quantified the uncertainties in
495 dust AAOD by using a non-parametric procedure based on the bootstrap
496 methodology^{87,88}. This propagates the uncertainties in each input dataset, including the
497 *in-situ* measurements, satellite-based, and reanalysis-derived dust properties, and the
498 spread in global model simulations used in DustCOMM. In addition, we used a similar
499 bootstrap methodology to quantify the uncertainties in our constraints on the dust
500 imaginary refractive index. We discuss the details of the framework used to constrain
501 dust refractive index and dust AAOD in the sub-sections below. In addition, we
502 compared our results with the dust-dominated aerosol refractive index and AAOD
503 retrieved from the ground-based AErosol RObotic NETwork (AERONET) and obtained
504 from several climate and chemical transport models.

505

506 **Constraints on the imaginary refractive index of North African dust at 550 nm
507 wavelength**

508 Dust refractive index is one of the key ingredients that determine dust AAOD (fig. S-1).
509 Because dust shortwave absorption depends more sensitively on the imaginary part of the
510 refractive index than on its real part^{15,31,60,61}, we focused on constraining the imaginary
511 dust refractive index. Specifically, we constrained the imaginary dust refractive index for
512 dust from both the Sahara and Sahel source regions by determining the values of these
513 two variables that optimally reproduced a compilation of 14 *in-situ* measurements of dust
514 single scattering albedo (SSA) over North Africa (Figure 2a). We compiled these dust
515 SSA measurements that used directly measured absorption and extinction coefficients
516 from major field campaigns taken over North Africa (see table S-1)^{23,41,53–59,94–96}. These
517 directly measured dust SSA measurements contrast indirect experimental dust SSA
518 estimates, which are usually based on Lorenz-Mie theory calculations that neglect dust
519 asphericity (see supplementary section S-1)^{97,98}. In contrast, the directly measured dust
520 SSA requires no assumption about dust shape and often has a lower uncertainty range
521 than the indirectly estimated dust SSA²³. We minimized the sum of squared differences
522 between these directly measured dust SSA estimates and our corresponding estimates of
523 dust SSA (cyan and pink/red bars in Figure 2a) to obtain constraints on the imaginary
524 refractive indices (k_r) of dust particles generated by the Sahara and the Sahel source
525 regions (pink/red bars in Figure 2c). That is:

$$526 \chi^2(k_r) = \sum_{j=1}^{N_j} \left[\text{SSA}_{\text{Measurement}}^j(\theta_j, \phi_j, t_j) - \text{SSA}_{\text{This Study}}^j(\theta_j, \phi_j, t_j) \right]^2, \quad (1)$$

527 where χ^2 is the cost function to minimize, with parameter bound for imaginary refractive
528 index at 550-nm wavelength between 10^{-4} and 10^{-2} ; $\text{SSA}_{\text{Measurement}}^j$ is the j^{th}
529 measurement in the compilation of *in-situ* dust SSA with a longitude, θ_j , latitude, ϕ_j ,
530 season t_j ; $N_j = 14$ is the total number of *in-situ* SSA measurements available (Table S-1).
531 The second parameter on the right of Eqn. 1 – $\text{SSA}_{\text{This Study}}^j$ – is the dust SSA calculated

532 for the same location and season as the j^{th} measurement (see supplementary section S-2
533 for details). In addition, the $SSA_{\text{This Study}}^j$ is estimated over the same location, altitude
534 range and diameter range as reported for the j^{th} measurement (see table S-1 for details).
535

536 To estimate $SSA_{\text{This Study}}^j$ and therefore obtain constraints on dust imaginary refractive
537 index (k_r), Eqn. 1 requires knowledge of three additional input parameters (see
538 supplementary section S-2). These input parameters are (1) the dust size distribution, (2)
539 the real part of dust refractive index, and (3) dust asphericity describing dust shape.

540 Because $SSA_{\text{This Study}}^j$ and k_r can vary substantially between the Sahara and Sahel dust
541 source regions, we also accounted for the difference in the optical properties of dust
542 generated by each of these two dust sources. Specifically, we accounted for the fractional
543 contribution by each dust source as a function of dust diameter to the overall dust
544 concentration at the measurement's location. This fractional contribution by each dust
545 source region was obtained by Kok et al.⁹³ as part of DustCOMM, which combined
546 observational constraints on dust properties and dust aerosol optical depth with an
547 ensemble of global model simulations. Consequently, we obtained the source-resolved
548 constraints on dust size distribution by multiplying the DustCOMM dust size distribution
549 with constraints on the fractional contribution by each dust source region to the overall
550 dust concentration (see Eqn. S-2.3). Therefore, we obtained the source-resolved
551 constraints on dust size distribution over the same height range and diameter range as
552 reported for the *in-situ* dust SSA measurements.
553

554 For the other two input parameters, we leveraged measurement-based estimates of dust
555 real refractive index and shape distribution of dust to determine $SSA_{\text{This Study}}^j$.

556 Specifically, we used the real dust refractive index, $n_r = 1.51 \pm 0.03$ (which is the same
557 for Sahara and Sahel) obtained from lab-based measurements of dust generated from
558 North African soil samples by Di Biagio et al.²⁹ (see their Table 4²⁹). Because the real
559 part of the dust refractive index has been shown to have smaller spatial and temporal
560 variability than the imaginary part^{29,58,63}, we used these lab-based measurements of dust
561 real refractive index to represent its value in the atmosphere. In addition, we accounted
562 for dust asphericity by using the source-invariant distributions of dust aspect ratio (AR;
563 length-to-width ratio) and height-to-width ratio (HWR) compiled by Huang et al.²⁷ using
564 measurements from dozens of studies. Since the Lorenz-Mie theory used in most global
565 models is invalid for aspherical dust particles, we obtained constraints on single-particle
566 optical properties that incorporate the effects of dust asphericity using the single-
567 scattering database of Meng et al.⁹⁹ (see supplementary section S-4). Therefore, with
568 these observationally informed constraints on dust size distribution, the real refractive
569 index, and dust asphericity, we estimated $SSA_{\text{This Study}}^j$ (see sections S-2 & S-3 for
570 details) and consequently obtained constraints on the dust imaginary refractive index (k_r)
571 by minimizing the sum of squared differences in Eqn. 1. Finally, we also quantified the
572 uncertainties in k_r using a bootstrap method^{87,88} that randomly selects (with replacement)
573 from the probability distributions of each of the input parameters (see supplementary
574 section S-5).
575

576 **Constraints on the absorption optical depth of North African dust at 550 nm**
 577 **wavelength**

578 We leveraged the constraint on dust imaginary refractive index (k_r) to obtain constraints
 579 on the absorption aerosol optical depth (AAOD) for North African dust at 550 nm
 580 wavelength (fig. S-1). Specifically, we obtained constraints on the size-resolved dust
 581 AAOD ($\hat{\tau}_{abs}$) for dust particles generated by the Sahara and Sahel source regions by
 582 obtaining constraints on column-integrated dust mass size distribution and the size-
 583 resolved dust mass absorption efficiency, which partially depends on dust refractive
 584 index (fig. S-1). That is:

$$585 \frac{d\hat{\tau}_{abs}(\theta, \phi, t, D)}{dD} = \sum_{r=1}^{N_r} \hat{\varepsilon}_{abs,asp}^r(n_r, k_r, AR, HWR, D) \cdot \frac{d\hat{M}^r(\theta, \phi, t, D)}{dD} \quad (2)$$

586 where, $\hat{\varepsilon}_{abs,asp}^r = \frac{3}{2\rho_d} \cdot \frac{\hat{Q}_{abs,asp}^r(n_r, k_r, AR, HWR, D)}{D}$ is the single-particle mass absorption
 587 efficiency ($m^2 g^{-1}$) for dust particles generated by each source region r , ($N_r = 2$, for
 588 Sahara and Sahel source regions; see Figure 2a). Here, we have assumed that the density
 589 of dust particles ($\rho_d = 2.5 \pm 0.2 \times 10^3 kg m^{-3}$) is independent of the dust source
 590 region, mineralogy, and dust diameter, $D^{3,100-102}$. Additionally, $\hat{Q}_{abs,asp}^r$ is the constraint
 591 on size-resolved single-particle dust absorption efficiency that varies as a function of
 592 source region r . It is defined as the absorption cross-section of the dust particle,
 593 normalized by the projected area of a sphere ($\pi D^2/4$) with diameter D (see
 594 supplementary section S-2 & S-4). The size-resolved $\hat{Q}_{abs,asp}^r$ and $\hat{\varepsilon}_{abs,asp}^r$ depend on the
 595 source-invariant constraints on the dust aspect ratio (AR; length-to-width ratio) and
 596 height-to-width ratio (HWR), the lab-based measurement of dust real refractive index
 597 (n_r), and our constraints source-resolved dust imaginary refractive indices (k_r). Since the
 598 Lorenz-Mie theory used in most global models is invalid for aspherical dust particles, we
 599 obtained constraints on $\hat{Q}_{abs,asp}^r$ (and other single-particle dust optical properties –
 600 $\hat{Q}_{sca,asp}^r$ and $\hat{Q}_{ext,asp}^r$) using the single-scattering database of Meng et al.⁹⁹ that
 601 incorporates the effects of dust asphericity on the dust optical property (see
 602 supplementary section S-4).

603

604 The second parameter on the right-hand side of Eqn. 2 – $\frac{d\hat{M}^r}{dD}$ – is the constraint on the
 605 contribution of each source region r to the column-integrated dust mass size distribution
 606 ($g m^{-3}$) at location θ, ϕ , during season t . Specifically, we obtained $\frac{d\hat{M}^r}{dD}$ by multiplying
 607 the constraints on the column-integrated dust mass loading (\hat{M}_{atm} ; $g m^{-2}$) with
 608 constraints on the column-integrated dust volume size distribution per source region
 609 ($\frac{d\hat{V}_Z^r}{dD}$). In turn, this constraint on the volume size distribution per source region ($\frac{d\hat{V}_Z^r}{dD}$) was
 610 calculated by multiplying the DustCOMM dust volume size distribution from Refs.^{3,21}
 611 with constraints on the fractional contribution by each dust source region to the size-
 612 resolved dust loading obtained from Kok et al.⁹³ (see Eqn. S-2.3). We normalized $\frac{d\hat{V}_Z^r}{dD}$

613 such that $\int_0^{D^{max}} \sum_{r=1}^{N_r} \frac{d\hat{V}_2^r}{dD} dD = 1$ over each location, with the upper limit of dust
614 diameter, $D^{max} = 20 \mu\text{m}$.

615

616 Overall, we used observationally informed constraints on dust loading, dust size
617 distribution, dust shape, and dust refractive index to obtain our constraints on source-
618 resolved size-resolved North African dust AAOD at 550 nm wavelength (Eqn. 1 and fig.
619 S-1). In addition, we also quantified the uncertainties in dust AAOD using a non-
620 parametric procedure based on the bootstrap method^{87,88} that randomly selects (with
621 replacement) from the probability distributions of each of the input parameters (see
622 supplementary section S-5). The probability distribution of the input parameters also
623 propagates the uncertainties in the different *in-situ* measurements, satellite-based and
624 reanalysis-derived dust properties, as well as due to the spread in the global aerosol
625 model simulations.

626

Dust optical properties obtained from selected models and from AeroCom models

We obtained dust absorption properties over North Africa, and the North Atlantic Ocean from two sets of global aerosol model simulations: (1) selected climate models, which include the Goddard Institute for Space Studies (GISS) ModelE general circulation model¹⁰³, the Weather Research and Forecasting model coupled with Chemistry (WRF-Chem), the Community Earth System Model (CESM)¹⁰⁴, Goddard Earth Observing System model coupled with Chemistry (GEOS-Chem), ARPEGE-Climate (CNRN)¹⁰⁵, and Integrated Massively Parallel Atmospheric Chemical Transport (IMPACT)¹⁰⁶ [see Table S-2 for details]; and (2) the AeroCom (Aerosol Comparison between Observations and Models) phase III models (details on the AeroCom models can be found in the references listed in Table S-2 and at <https://wiki.met.no/aerocom/phase3-experiments>). From these two sets of models, we obtained the following spatially-varying seasonally averaged dust properties: from the selected models, we obtained height-resolved and size-resolved dust mass loading²¹, while from the AeroCom models, we obtained the column-integrated dust AAOD and total AAOD¹⁴.

Using these variables, we calculated other dust properties that are not part of these model simulations but are required for comparisons made in this study. For example, since dust AAOD is only available for AeroCom models, we estimated the dust AAOD for the selected models using the size-resolved dust mass loading and the dust refractive index assumed in each model (see Table S-2). In addition, to compare model simulations with the *in-situ* dust SSA measurements, we calculated the dust SSA for the Selected and AeroCom models using each model's assumed dust refractive index and simulated dust size distribution over the same height range and diameter range as the *in-situ* dust SSA measurements (Table S-1). Details of the procedures to calculate the dust aerosol absorption optical depth and the dust single-scattering albedo for selected models and AeroCom models are described in supplementary section S-6.

In addition, to understand the contribution of dust imaginary refractive index and size-resolved dust properties on the overall bias in simulated dust AAOD (Figure 4a), we replaced the input parameters in the calculation of dust AAOD (Eqn. 2) for each of the

658 six Selected models with the constraints obtained in this study (see section S-6 for
659 details). Specifically, for the contribution of size-resolved dust properties, we replaced
660 simulated source-resolved dust size distribution ($\frac{d\hat{V}_m^r}{dD}$; where m_s represent each Selectd
661 model), source-resolved column-integrated dust mass load ($\tilde{M}_{m_s}^r$) by the corresponding
662 constraints obtained from this study (that is $\frac{d\hat{V}_Z^r}{dD}$ and \hat{M}_{atm} respectively). In addition, the
663 spherical representation of dust shape is replaced by an aspherical representation obtained
664 by the measurement compilation of Huang et al.²⁷ of the dust aspect ratio (AR) and
665 height-to-width ratio (HWR) used in the calculation of single-particle dust optical
666 properties. Furthermore, for the contribution of dust imaginary refractive index, we
667 replaced the source-invariant values assumed for each model (i.e., k^{m_s} see Table S-2)
668 with our source-resolved estimates (k_r). We also replace the real part of the imaginary
669 refractive index (n^{m_s}), with the lab-based estimates (n_r) from Di Biagio et al.²⁹.
670 Therefore, the difference between these mode-based estimates and our constraints shows
671 the contribution of that the input parameter on the simulated dust AAOD. Given the non-
672 linear, non-additive nature of this procedure and the parameters, the combined effect of
673 contributions does not directly reproduce the overall bias, indicating that the residual is
674 non-zero (see Figure 4a).
675

676 **Dust optical properties obtained from AERONET.**

677 We obtained aerosol absorption optical depth, size distribution, and complex refractive
678 index from AERONET (AErosol RObotic NETwork). While details about the AERONET
679 project, its instrumentations, and retrieval algorithm can be found elsewhere in the
680 literature^{36,37}, we provide here a brief overview. AERONET provides global ground-based
681 remote-sensing observations of aerosol extinction and retrieval of other atmospheric
682 aerosol properties³⁹. Specifically, each AERONET station is equipped with an automatic
683 sun and sky scanning radiometer that measures the direct solar intensity and almucantar
684 sky radiance, which are used to obtain the total column aerosol optical depth for at least
685 the four main wavelengths (including 440, 670, 870, and 1020 nm)¹⁰⁷. The spectral aerosol
686 optical depth and the spectral sky radiances, through an inversion algorithm^{36,37}, are used
687 to obtain column integrated aerosol size distribution, complex index of refraction, and
688 subsequently the single-scattering albedo (SSA) and the aerosol absorption optical depth
689 (AAOD).

690 We used AERONET version-3 aerosol properties, which include substantial improvements
691 to the retrieval algorithm compared to the previous versions. Details of these improvements
692 in version-3 can be found in Giles et al.¹⁰⁸ and Sinyuk et al.⁹¹. The level-2.0 of version-3
693 datasets applies additional quality control criteria relative to the level-1.5 datasets.
694 Specifically, level-2.0 requires the solar zenith angle to be greater than 50 degrees and the
695 aerosol optical depth at 440 nm to be greater than 0.4^{91,108}. Because these additional quality
696 control criteria substantially reduce the number of available measurements by excluding
697 days with low aerosol concentration and locations farther from the major sources over
698 North Africa, it may result in bias in the retrieved aerosol properties. To minimize this bias,
699 we follow Bond et al.⁸⁰ and combined level-2.0 with the level-1.5 dataset, only using level-
700 1.5 for days where level-2.0 is not available.

Furthermore, since AERONET reports the total aerosol properties and does not discriminate between aerosol species, we applied additional constraints to select the stations and retrievals that are dominated by dust aerosols over North Africa. First, we selected only days with measurements that have an extinction angstrom exponent less than 0.2 using wavelengths of 440 and 870 nm^{47,61,109} ($AE \leq 0.2$). We do so because $AE \leq 0.2$ better represents 'pure dust'¹¹⁰, which further helps to discriminate dust from other non-dust aerosols and have enough measurements for a statistically significant analysis over North Africa. Although some previous studies have used different values of angstrom exponent (both above and below $AE=0.2$) to discriminate dust from non-dust aerosols^{18,109,111}, our selection here does not change the conclusion presented in this study (see fig. S-5). For example, using a lower angstrom exponent of 0.1 still results in an overestimation of AERONET-retrieved AAOD, which is still associated with higher refractive index (although less than when $AE \leq 0.2$) and lower coarse dust load (although higher than when $AE \leq 0.2$), when compared to our estimates over North Africa. Second, to further improve the validity of our estimates and reduce the uncertainties in the climatological averages that we compared, we required that each monthly average contains retrievable information for at least ten (10) days in each month, with at least two (2) months of available data for the seasonal averages⁸⁰. Third, we selected AERONET stations whose measurements are likely dominated by dust aerosols. To do so, we used MERRA-2 reanalysis aerosol properties¹¹² to select only stations where the percentage contribution of dust extinction to the climatological total aerosol extinction is more than 60 % (see fig. S-6). In addition, to avoid coastal stations with substantial contamination from sea salt in the boundary layer, we used the threshold that the climatological contribution of sea-salt aerosols to the total aerosol surface concentration (which include black and organic carbons, DMS, SO₂, SO₄, and dust aerosols) should be less than 20 % for each station (see fig. S-6). Fourth, to account for the non-linearity in the spectral variation of imaginary refractive index and AAOD, we use a second order fit of the logarithm of AERONET-retrieved imaginary refractive index and AAOD versus logarithm of the wavelength to interpolate their respective values at 550 nm wavelength^{63–65}. Finally, to put the AERONET retrievals on a similar footing with our constraints and ensemble of model simulations, we calculated the climatological average of the quality-controlled AERONET retrievals over each location.

733

734 **Limitations of our methodology**

735 Although we quantified the uncertainties in our constraints on dust imaginary refractive
736 index (k_r ; Eqn. 1) and dust AAOD (\hat{t}_{abs} ; Eqn. 2), our methodology is still subject to some
737 important limitations. First, limitations in instrumentation resulted in a compilation of *in-situ*
738 dust SSA measurements that may not adequately account for the full range of particle
739 sizes observed over North Africa. Although airborne dust particles with a diameter larger
740 than 50 μm have been measured over North Africa^{20,23,55,113,114}, most of our dust SSA
741 measurements are taken by airborne nephelometers and Particle Soot Absorption
742 Photometers with sub-micron diameter cut-off less than $\sim 3 \mu\text{m}$ ^{23,41,53–56}. Only a few of the
743 dust SSA measurements account for particles larger than 3 μm diameter (Table S-1)^{57–}
744 ^{59,95,96}. We mitigated this issue by matching the diameter range in the calculation of dust
745 SSA ($\text{SSA}_{\text{This Study}}^j$; Eqn. 1 & Eqn. S2.1) to the diameter range captured by each
746 measurement.

747
748 The second limitation is that additional uncertainties may be introduced into our estimates
749 through inherent uncertainties associated with our methodology and the input datasets,
750 including uncertainties in DustCOMM dust size distribution, dust loading, and the
751 fractional contribution of each dust source. For example, methodological uncertainties may
752 be introduced through the representative location and height range used for dust SSA
753 measurements. Although we used the reported location and height range, we assigned a
754 representative location to each dust SSA measurement based on the reported locations over
755 which the data was taken (see section S-1). In addition, to constrain dust imaginary
756 refractive index, we used seasonally averaged DustCOMM dust size distribution that
757 corresponds to the measurement's season. However, the dust size distribution for a
758 representative season and location may not necessarily reflect the condition of the specific
759 date(s) when the measurement was taken.
760

761 Furthermore, other inherent uncertainties associated with DustCOMM dust size
762 distribution may be introduced into our analysis (Eqn. 2). Specifically, although dust
763 particles with $D \geq 20 \mu\text{m}$ have also been measured for North African dust^{20,23,55,113,114},
764 their inclusion in DustCOMM dust size distribution may result in large uncertainties
765 because such measurements are still relatively scarce^{3,21}. As a result, we also avoided such
766 large uncertainties in our constraints on dust AAOD. In addition, most climate and
767 chemical transport models, including those highlighted in this study, also don't account for
768 dust with $D \geq 20 \mu\text{m}$, and the majority have dust with a maximum diameter of $10 \mu\text{m}$ ^{14,115}.
769

770 An additional limitation is that our constraints on dust AAOD only accounted for the
771 contributions from Sahara and Sahel sources. However, Kok et al.⁵⁰ highlighted that the
772 sources over the Middle East and Central Asian regions contribute to dust aerosols reaching
773 locations over North Africa. Although this contribution is small (about 7.5 %) relative to
774 the Sahara and the Sahel regions, it could introduce non-negligible uncertainties in the
775 source-resolved dust mass distribution and, consequently, on our constraints on dust
776 AAOD. Furthermore, our methodology did not account for the effect of aging on the
777 composition of dust and, consequently, the dust refractive index as it is transported from
778 the source regions¹¹⁶. However, previous studies with *in-situ* measurements pointed to
779 little changes in the optical properties of dust plumes as they are transported from North
780 African sources^{114,117}, thus suggesting that the effect of aging in our estimate of dust
781 AAOD is likely small.
782

783 **Data and materials availability:** Dust absorption properties from AeroCom models are
784 obtained from the repository at <http://aerocom.met.no> (last assessed on January 2020),
785 and AERONET-retrieved aerosol absorption properties are obtained from
786 <https://aeronet.gsfc.nasa.gov> (last assessed on June 2021). Previously published datasets,
787 such as dust properties from the selected models and DustCOMM datasets, are available
788 through cited publications^{118–120}. Our constraints on dust imaginary refractive index and
789 dust absorption aerosol optical depth as well as the code used to obtain these datasets are
790 publicly available at ref¹²¹ (<https://doi.org/10.5281/zenodo.6406831>).
791

792 **Code availability**

793 Code used to generate the dust single-scattering albedo, the dust imaginary refractive
794 index and dust AAOD are available at ref¹²¹ (<https://doi.org/10.5281/zenodo.6406831>).
795 Matlab was used for data generation, but all figures except Figure 1 are made using
796 National Center for Atmospheric Research (NCAR) Command Line (NCL;
797 <https://www.ncl.ucar.edu/>).

798

799

800 **Acknowledgements**

801 We thank the groups that participated in the AeroCom phase III experiments and
802 contributed to the models used in this study. In addition, we are also thankful to the PIs
803 and staff that maintain all the AERONET sites used in this study. We also thank Gregory
804 Schuster and Dirk Olivié for helpful comments on the manuscript. **Funding:** A.A.A was
805 supported by Department of Energy's Research Development and Partnership Pilot
806 program grant DE-SC0023033, the University of California – Merced, and the University
807 of California Office of the President. Y. H. acknowledged financial support from
808 Columbia University Earth Institute Postdoctoral Research Fellowship and the NASA
809 grant 80NSSC19K1346, awarded under the Future Investigators in NASA Earth and
810 Space Science and Technology (FINESST) program. J. F. K. acknowledged support from
811 the National Science Foundation (NSF) grants 1552519 and 1856389 and from the Army
812 Research Office under Cooperative Agreement Number W911NF-20-2-0150. The views
813 and conclusions contained in this document are those of the authors and should not be
814 interpreted as representing the official policies, either expressed or implied, of the Army
815 Research Laboratory or the U.S. Government. B.H.S acknowledged funding from the
816 Research Council of Norway through the project ARIDITY (324556).

817

818 **Author Contributions:** A.A.A led the research project, which both A.A.A and J.F.K
819 designed; B.H.S provided access to the AeroCom datasets, and Y.H estimated the single-
820 particle optical properties used in the study. A.A.A performed the research, analyzed the
821 data, and wrote the paper. All authors discussed the results and provided comments.

822

823 **Competing Interest Statement:** The authors declare that they have no competing
824 financial and non-financial interests.

825

826

827 **References:**

828 1. Boucher, O. et al. Clouds and Aerosols. *Climate Change 2013: The Physical Science*
829 Basis. Contribution of Working Group I to the Fifth Assessment Report of the
830 Intergovernmental Panel on Climate Change 571–657 (2013)
831 doi:10.1017/CBO9781107415324.016.

832 2. Bellouin, N. et al. Bounding Global Aerosol Radiative Forcing of Climate Change.
833 *Reviews of Geophysics* vol. 58 Preprint at <https://doi.org/10.1029/2019RG000660>
834 (2020).

835 3. Adebiyi, A. A. & Kok, J. F. Climate models miss most of the coarse dust in the
836 atmosphere. *Science Advances* **6**, eaaz9507 (2020).

837 4. Haywood, J. M. & Shine, K. P. The effect of anthropogenic sulfate and soot aerosol
838 on the clear sky planetary radiation budget. *Geophysical Research Letters* **22**, 603–
839 606 (1995).

840 5. Di Biagio, C., Balkanski, Y., Albani, S., Boucher, O. & Formenti, P. Direct Radiative
841 Effect by Mineral Dust Aerosols Constrained by New Microphysical and Spectral
842 Optical Data. *Geophysical Research Letters* **47**, (2020).

843 6. Kok, J. F., Ward, D. S., Mahowald, N. M. & Evan, A. T. Global and regional
844 importance of the direct dust-climate feedback. *Nature Communications* **9**, 241
845 (2018).

846 7. Perlitz, J. & Miller, R. L. Cloud cover increase with increasing aerosol absorptivity:
847 A counterexample to the conventional semidirect aerosol effect. *Journal of*
848 *Geophysical Research: Atmospheres* **115**, 1–23 (2010).

849 8. Amiri-Farahani, A., Allen, J. R., Neubauer, D. & Lohmann, U. Impact of Saharan
850 dust on North Atlantic marine stratocumulus clouds: Importance of the semidirect
851 effect. *Atmospheric Chemistry and Physics* **17**, 6305–6322 (2017).

852 9. Huang, J., Wang, T., Wang, W., Li, Z. & Yan, H. Climate effects of dust aerosols
853 over east asian arid and semiarid regions. *Journal of Geophysical Research Preprint*
854 at <https://doi.org/10.1002/2014JD021796> (2014).

855 10. Reale, O., Lau, K. M., Da Silva, a. & Matsui, T. Impact of assimilated and
856 interactive aerosol on tropical cyclogenesis. *Geophysical Research Letters* **41**,
857 3282–3288 (2014).

858 11. Dunion, J. P. & Velden, C. S. The impact of the Saharan Air Layer on Atlantic
859 tropical cyclone activity. *Bulletin of the American Meteorological Society* **85**, 353–
860 365 (2004).

861 12. Samset, B. H. et al. Aerosol Absorption: Progress Towards Global and Regional
862 Constraints. *Current Climate Change Reports* **4**, 65–83 (2018).

863 13. Li, L. et al. Quantifying the range of the dust direct radiative effect due to source
864 mineralogy uncertainty. *Atmospheric Chemistry and Physics* **21**, 3973–4005 (2021).

865 14. Sand, M. et al. Aerosol absorption in global models from AeroCom phase III.
866 *Atmospheric Chemistry and Physics* **21**, 15929–15947 (2021).

867 15. Bergstrom, R. W. et al. Spectral absorption properties of atmospheric aerosols.
868 *Atmospheric Chemistry and Physics* **7**, 5937–5943 (2007).

869 16. Ridley, D. A., Heald, C. L., Kok, J. F. & Zhao, C. An observationally constrained
870 estimate of global dust aerosol optical depth. *Atmospheric Chemistry and Physics*
871 **16**, 15097–15117 (2016).

872 17. Song, Q., Zhang, Z., Yu, H., Ginoux, P. & Shen, J. Global dust optical depth
873 climatology derived from CALIOP and MODIS aerosol retrievals on decadal
874 timescales: regional and interannual variability. *Atmospheric Chemistry and Physics*
875 **21**, 13369–13395 (2021).

876 18. Huneeus, N. et al. Global dust model intercomparison in AeroCom phase i.
877 *Atmospheric Chemistry and Physics* **11**, 7781–7816 (2011).

878 19. Kok, J. F. A scaling theory for the size distribution of emitted dust aerosols suggests
879 climate models underestimate the size of the global dust cycle. *Proceedings of the*
880 *National Academy of Sciences* **108**, 1016–1021 (2011).

881 20. Ryder, C. L. et al. Coarse and giant particles are ubiquitous in Saharan dust export
882 regions and are radiatively significant over the Sahara. *Atmospheric Chemistry and*
883 *Physics* **19**, 15353–15376 (2019).

884 21. Adebiyi, A. A. et al. Dust Constraints from joint Observational-Modelling-
885 experiMental analysis (DustCOMM): comparison with measurements and model
886 simulations. *Atmospheric Chemistry and Physics* **20**, 829–863 (2020).

887 22. Otto, S., Trautmann, T. & Wendisch, M. On realistic size equivalence and shape of
888 spheroidal Saharan mineral dust particles applied in solar and thermal radiative
889 transfer calculations. *Atmospheric Chemistry and Physics* **11**, 4469–4490 (2011).

890 23. Ryder, C. L. et al. Coarse-mode mineral dust size distributions, composition and
891 optical properties from AER-D aircraft measurements over the tropical eastern
892 Atlantic. *Atmospheric Chemistry and Physics* **18**, 17225–17257 (2018).

893 24. Ansmann, A. et al. Profiling of Saharan dust from the Caribbean to western Africa –
894 Part 2: Shipborne lidar measurements versus forecasts. *Atmospheric Chemistry and*
895 *Physics* **17**, 14987–15006 (2017).

896 25. Yang, P. et al. Modeling of the scattering and radiative properties of nonspherical
897 dust-like aerosols. *Journal of Aerosol Science* **38**, 995–1014 (2007).

898 26. Kalashnikova, O. V. & Sokolik, I. N. Modeling the radiative properties of
899 nonspherical soil-derived mineral aerosols. *Journal of Quantitative Spectroscopy*
900 and Radiative Transfer **87**, 137–166 (2004).

901 27. Huang, Y. et al. Climate Models and Remote Sensing Retrievals Neglect Substantial
902 Desert Dust Asphericity. *Geophysical Research Letters* **47**, (2020).

903 28. Formenti, P. et al. Dominance of goethite over hematite in iron oxides of mineral dust
904 from Western Africa: Quantitative partitioning by X-ray absorption spectroscopy.
905 *Journal of Geophysical Research: Atmospheres* **119**, 12,740–12,754 (2014).

906 29. Di Biagio, C. et al. Complex refractive indices and single-scattering albedo of global
907 dust aerosols in the shortwave spectrum and relationship to size and iron content.
908 *Atmospheric Chemistry and Physics* **19**, 15503–15531 (2019).

909 30. Claquin, T., Schulz, M. & Balkanski, Y. J. Modeling the mineralogy of atmospheric
910 dust sources. *Journal of Geophysical Research Atmospheres* **104**, 22243–22256
911 (1999).

912 31. Moosmüller, H. et al. Single scattering albedo of fine mineral dust aerosols controlled
913 by iron concentration. *Journal of Geophysical Research: Atmospheres* **117**, n/a–n/a
914 (2012).

915 32. Journet, E., Balkanski, Y. & Harrison, S. P. A new data set of soil mineralogy for
916 dust-cycle modeling. *Atmospheric Chemistry and Physics* **14**, 3801–3816 (2014).

917 33. Nickovic, S., Vukovic, A., Vujadinovic, M., Djurdjevic, V. & Pejanovic, G.
918 Technical Note: High-resolution mineralogical database of dust-productive soils for
919 atmospheric dust modeling. *Atmospheric Chemistry and Physics* **12**, 845–855
920 (2012).

921 34. Zender, C. S., Bian, H. & Newman, D. Mineral Dust Entrainment and Deposition
922 (DEAD) model: Description and 1990s dust climatology. *Journal of Geophysical*
923 *Research* **108**, 4416 (2003).

924 35. Perlitz, J. P., Pérez García-Pando, C. & Miller, R. L. Predicting the mineral
925 composition of dust aerosols – Part 1: Representing key processes. *Atmospheric*
926 *Chemistry and Physics* **15**, 11593–11627 (2015).

927 36. Dubovik, O. & King, M. D. A flexible inversion algorithm for retrieval of aerosol
928 optical properties from Sun and sky radiance measurements. *Journal of Geophysical*
929 *Research: Atmospheres* **105**, 20673–20696 (2000).

930 37. Dubovik, O. et al. Application of spheroid models to account for aerosol particle
931 nonsphericity in remote sensing of desert dust. *Journal of Geophysical Research*
932 **111**, D11208 (2006).

933 38. Giles, D. M. et al. An analysis of AERONET aerosol absorption properties and
934 classifications representative of aerosol source regions. *Journal of Geophysical*
935 *Research: Atmospheres* **117**, n/a-n/a (2012).

936 39. Holben, B. N. et al. AERONET—A Federated Instrument Network and Data Archive
937 for Aerosol Characterization. *Remote Sensing of Environment* **66**, 1–16 (1998).

938 40. Ryder, C. L. et al. Advances in understanding mineral dust and boundary layer
939 processes over the Sahara from Fennec aircraft observations. *Atmospheric*
940 *Chemistry and Physics* **15**, 8479–8520 (2015).

941 41. McConnell, C. L. et al. Seasonal variations of the physical and optical characteristics
942 of Saharan dust: Results from the Dust Outflow and Deposition to the Ocean
943 (DODO) experiment. *Journal of Geophysical Research* **113**, 14S05 (2008).

944 42. Müller, D. et al. Mineral dust observed with AERONET Sun photometer, Raman
945 lidar, and in situ instruments during SAMUM 2006: Shape-independent particle
946 properties. *Journal of Geophysical Research* **115**, D07202 (2010).

947 43. Müller, D. et al. Comparison of optical and microphysical properties of pure Saharan
948 mineral dust observed with AERONET Sun photometer, Raman lidar, and in situ
949 instruments during SAMUM 2006. *Journal of Geophysical Research: Atmospheres*
950 **117**, n/a-n/a (2012).

951 44. Solmon, F. et al. Dust aerosol impact on regional precipitation over western Africa,
952 mechanisms and sensitivity to absorption properties. *Geophysical Research Letters*
953 **35**, L24705 (2008).

954 45. Strong, J. D. O., Vecchi, G. A. & Ginoux, P. The Climatological Effect of Saharan
955 Dust on Global Tropical Cyclones in a Fully Coupled GCM. *Journal of Geophysical*
956 *Research: Atmospheres* **123**, 5538–5559 (2018).

957 46. Kinne, S. The MACv2 aerosol climatology. *Tellus B: Chemical and Physical*
958 *Meteorology* **71**, 1–21 (2019).

959 47. Russell, P. B. et al. Absorption Angstrom Exponent in AERONET and related data as
960 an indicator of aerosol composition. *Atmospheric Chemistry and Physics* **10**, 1155–
961 1169 (2010).

962 48. Caponi, L. et al. Spectral- and size-resolved mass absorption efficiency of mineral
963 dust aerosols in the shortwave spectrum: A simulation chamber study. *Atmospheric*
964 *Chemistry and Physics* **17**, 7175–7191 (2017).

965 49. Ginoux, P., Prospero, J. M., Gill, T. E., Hsu, N. C. & Zhao, M. Global-scale
966 attribution of anthropogenic and natural dust sources and their emission rates based
967 on MODIS Deep Blue aerosol products. *Reviews of Geophysics* vol. 50 Preprint at
968 <https://doi.org/10.1029/2012RG000388> (2012).

969 50. Kok, J. F. et al. Contribution of the world's main dust source regions to the global
970 cycle of desert dust. *Atmospheric Chemistry and Physics* **21**, 8169–8193 (2021).

971 51. Knippertz, P. & Stuut, J.-B. *Mineral Dust*. (Springer Netherlands, 2014).
972 doi:10.1007/978-94-017-8978-3.

973 52. Bevington, P. R., Robinson, D. ~K. K., Blair, J. M., Mallinckrodt, A. J. & McKay, S.
974 Data Reduction and Error Analysis for the Physical Sciences. *Computers in Physics*
975 **7**, 415 (1993).

976 53. Haywood, J. et al. Radiative properties and direct effect of Saharan dust measured by
977 the C-130 aircraft during Saharan Dust Experiment (SHADE): 2. Terrestrial
978 spectrum. *Journal of Geophysical Research* **108**, 8578 (2003).

979 54. Osborne, S. R. et al. Physical and optical properties of mineral dust aerosol during the
980 Dust and Biomass-burning Experiment. *Journal of Geophysical Research* **113**,
981 00C03 (2008).

982 55. Johnson, B. T. & Osborne, S. R. Physical and optical properties of mineral dust
983 aerosol measured by aircraft during the GERBILS campaign. *Quarterly Journal of*
984 *the Royal Meteorological Society* **137**, 1117–1130 (2011).

985 56. Ryder, C. L. et al. Optical properties of Saharan dust aerosol and contribution from
986 the coarse mode as measured during the Fennec 2011 aircraft campaign.
987 *Atmospheric Chemistry and Physics* **13**, 303–325 (2013).

988 57. Schladitz, A. et al. In situ measurements of optical properties at Tinfou (Morocco)
989 during the Saharan Mineral Dust Experiment SAMUM 2006. *Tellus, Series B:*
990 *Chemical and Physical Meteorology* **61**, 64–78 (2009).

991 58. Formenti, P. et al. Airborne observations of mineral dust over western Africa in the
992 summer Monsoon season: spatial and vertical variability of physico-chemical and
993 optical properties. *Atmospheric Chemistry and Physics* **11**, 6387–6410 (2011).

994 59. Müller, T., Schladitz, A., Kandler, K. & Wiedensohler, A. Spectral particle
995 absorption coefficients, single scattering albedos and imaginary parts of refractive
996 indices from ground based in situ measurements at Cape Verde Island during
997 SAMUM-2. *Tellus, Series B: Chemical and Physical Meteorology* **63**, 573–588
998 (2011).

999 60. Haywood, J. M., Francis, P. N., Glew, M. D. & Taylor, J. P. Optical properties and
1000 direct radiative effect of Saharan dust: A case study of two Saharan dust outbreaks
1001 using aircraft data. *Journal of Geophysical Research: Atmospheres* **106**, 18417–
1002 18430 (2001).

1003 61. Sinyuk, A., Torres, O. & Dubovik, O. Combined use of satellite and surface
1004 observations to infer the imaginary part of refractive index of Saharan dust.
1005 *Geophysical Research Letters* **30**, (2003).

1006 62. Engelbrecht, J. P. et al. Technical note: Mineralogical, chemical, morphological, and
1007 optical interrelationships of mineral dust re-suspensions. *Atmospheric Chemistry*
1008 and *Physics* **16**, 10809–10830 (2016).

1009 63. Wagner, R. et al. Complex refractive indices of Saharan dust samples at visible and
1010 near UV wavelengths: a laboratory study. *Atmospheric Chemistry and Physics* **12**,
1011 2491–2512 (2012).

1012 64. Eck, T. F. et al. Wavelength dependence of the optical depth of biomass burning,
1013 urban, and desert dust aerosols. *Journal of Geophysical Research: Atmospheres* **104**,
1014 31333–31349 (1999).

1015 65. Müller, D. et al. Comparison of optical and microphysical properties of pure Saharan
1016 mineral dust observed with AERONET Sun photometer, Raman lidar, and in situ
1017 instruments during SAMUM 2006. *Journal of Geophysical Research: Atmospheres*
1018 **117**, n/a-n/a (2012).

1019 66. Otto, S. et al. Atmospheric radiative effects of an in situ measured Saharan dust
1020 plume and the role of large particles. *Atmospheric Chemistry and Physics* **7**, 4887–
1021 4903 (2007).

1022 67. Balkanski, Y., Schulz, M., Clauquin, T. & Guibert, S. Reevaluation of Mineral aerosol
1023 radiative forcings suggests a better agreement with satellite and AERONET data.
1024 *Atmospheric Chemistry and Physics* **7**, 81–95 (2007).

1025 68. Scanza, R. A. et al. Modeling dust as component minerals in the Community
1026 Atmosphere Model: development of framework and impact on radiative forcing.
1027 *Atmospheric Chemistry and Physics* **15**, 537–561 (2015).

1028 69. Albani, S. et al. Improved dust representation in the Community Atmosphere Model.
1029 *Journal of Advances in Modeling Earth Systems* **6**, 541–570 (2014).

1030 70. Mahowald, N. et al. The size distribution of desert dust aerosols and its impact on the
1031 Earth system. *Aeolian Research* **15**, 53–71 (2014).

1032 71. Li, L. & Sokolik, I. N. The Dust Direct Radiative Impact and Its Sensitivity to the
1033 Land Surface State and Key Minerals in the WRF-Chem-DuMo Model: A Case
1034 Study of Dust Storms in Central Asia. *Journal of Geophysical Research:*
1035 *Atmospheres* **123**, 4564–4582 (2018).

1036 72. Balkanski, Y., Bonnet, R., Boucher, O., Checa-Garcia, R. & Servonnat, J. Better
1037 representation of dust can improve climate models with too weak an African
1038 monsoon. *Atmospheric Chemistry and Physics* **21**, 11423–11435 (2021).

1039 73. O’Sullivan, D. et al. Models transport Saharan dust too low in the atmosphere: A
1040 comparison of the MetUM and CAMS forecasts with observations. *Atmospheric*
1041 *Chemistry and Physics* **20**, 12955–12982 (2020).

1042 74. Myriokefalitakis, S. et al. Reviews and syntheses: The GESAMP atmospheric iron
1043 deposition model intercomparison study. *Biogeosciences* vol. 15 6659–6684
1044 Preprint at <https://doi.org/10.5194/bg-15-6659-2018> (2018).

1045 75. Hamilton, D. S. et al. Improved methodologies for Earth system modelling of
1046 atmospheric soluble iron and observation comparisons using the Mechanism of
1047 Intermediate complexity for Modelling Iron (MIMI v1.0). *Geoscientific Model*
1048 *Development* **12**, 3835–3862 (2019).

1049 76. Conway, T. M. et al. Tracing and constraining anthropogenic aerosol iron fluxes to
1050 the North Atlantic Ocean using iron isotopes. *Nature Communications* **10**, 1–10
1051 (2019).

1052 77. Omar, A. H. et al. The CALIPSO automated aerosol classification and lidar ratio
1053 selection algorithm. *Journal of Atmospheric and Oceanic Technology* **26**, 1994–
1054 2014 (2009).

1055 78. Tesche, M. et al. Ground-based validation of CALIPSO observations of dust and
1056 smoke in the Cape Verde region. *Journal of Geophysical Research: Atmospheres*
1057 **118**, 2889–2902 (2013).

1058 79. Wandinger, U. et al. Size matters: Influence of multiple scattering on CALIPSO
1059 light-extinction profiling in desert dust. *Geophysical Research Letters* **37**, n/a-n/a
1060 (2010).

1061 80. Bond, T. C. et al. Bounding the role of black carbon in the climate system: A
1062 scientific assessment. *Journal of Geophysical Research Atmospheres* **118**, 5380–
1063 5552 (2013).

1064 81. Adebiyi, A. et al. A review of coarse mineral dust in the Earth system. *Aeolian
1065 Research* **60**, 100849 (2023).

1066 82. Johnson, B. T. & Osborne, S. R. Physical and optical properties of mineral dust
1067 aerosol measured by aircraft during the GERBILS campaign. *Quarterly Journal of
1068 the Royal Meteorological Society* **137**, 1117–1130 (2011).

1069 83. Formenti, P. et al. Airborne observations of mineral dust over western Africa in the
1070 summer Monsoon season: spatial and vertical variability of physico-chemical and
1071 optical properties. *Atmospheric Chemistry and Physics* **11**, 6387–6410 (2011).

1072 84. Ryder, C. L. et al. Coarse-mode mineral dust size distributions, composition and
1073 optical properties from AER-D aircraft measurements over the tropical eastern
1074 Atlantic. *Atmospheric Chemistry and Physics* **18**, 17225–17257 (2018).

1075 85. Quinn, P. K. et al. Aerosol optical properties during INDOEX 1999: Means,
1076 variability, and controlling factors. *Journal of Geophysical Research* **107**, 8020–
1077 8020 (2002).

1078 86. Weinzierl, B. et al. Airborne measurements of dust layer properties, particle size
1079 distribution and mixing state of Saharan dust during SAMUM 2006. *Tellus B:
1080 Chemical and Physical Meteorology* **61**, 96–117 (2009).

1081 87. Efron, B. & Gong, G. A Leisurely Look at the Bootstrap, the Jackknife, and Cross-
1082 Validation. *The American Statistician* **37**, 36–48 (1983).

1083 88. Chernick, M. R. *Bootstrap Methods. Climate Change 2013 - The Physical Science
1084 Basis* vol. 53 (John Wiley & Sons, Inc., 2007).

1085 89. Holben, B. N. et al. Aeronet's Version 2.0 quality assurance criteria. in *Remote
1086 Sensing of the Atmosphere and Clouds* (eds. Tsay, S.-C., Nakajima, T., Singh, R. P.
1087 & Sridharan, R.) vol. 6408 64080Q-64080Q (SPIE, 2006).

1088 90. Dubovik, O. et al. Accuracy assessments of aerosol optical properties retrieved from
1089 Aerosol Robotic Network (AERONET) Sun and sky radiance measurements.
1090 *Journal of Geophysical Research: Atmospheres* **105**, 9791–9806 (2000).

1091 91. Sinyuk, A. et al. The AERONET Version 3 aerosol retrieval algorithm, associated
1092 uncertainties and comparisons to Version 2. *Atmospheric Measurement Techniques*
1093 **13**, 3375–3411 (2020).

1094 92. Engelstaedter, S., Tegen, I. & Washington, R. North African dust emissions and
1095 transport. *Earth-Science Reviews* **79**, 73–100 (2006).

1096 93. Kok, J. F. et al. Improved representation of the global dust cycle using observational
1097 constraints on dust properties and abundance. *Atmospheric Chemistry and Physics*
1098 **21**, 8127–8167 (2021).

1099 94. Chen, G. et al. Observations of Saharan dust microphysical and optical properties
1100 from the Eastern Atlantic during NAMMA airborne field campaign. *Atmospheric*
1101 *Chemistry and Physics* **11**, 723–740 (2011).

1102 95. Denjean, C. et al. Size distribution and optical properties of African mineral dust after
1103 intercontinental transport. *Journal of Geophysical Research: Atmospheres* **121**,
1104 7117–7138 (2016).

1105 96. Denjean, C. et al. Overview of aerosol optical properties over southern West Africa
1106 from DACCIWA aircraft measurements. *Atmospheric Chemistry and Physics* **20**,
1107 4735–4756 (2020).

1108 97. Clarke, A. D. et al. Size distributions and mixtures of dust and black carbon aerosol
1109 in Asian outflow: Physiochemistry and optical properties. *Journal of Geophysical*
1110 *Research* **109**, 15S09 (2004).

1111 98. Otto, S. et al. Solar radiative effects of a Saharan dust plume observed during
1112 SAMUM assuming spheroidal model particles. *Tellus, Series B: Chemical and*
1113 *Physical Meteorology* **61**, 270–296 (2009).

1114 99. Meng, Z. et al. Single-scattering properties of tri-axial ellipsoidal mineral dust
1115 aerosols: A database for application to radiative transfer calculations. *Journal of*
1116 *Aerosol Science* **41**, 501–512 (2010).

1117 100. Kok, J. F. et al. Smaller desert dust cooling effect estimated from analysis of dust
1118 size and abundance. *Nature Geoscience* **10**, 274–278 (2017).

1119 101. Kaaden, N. et al. State of mixing, shape factor, number size distribution, and
1120 hygroscopic growth of the Saharan anthropogenic and mineral dust aerosol at
1121 Tinfou, Morocco. *Tellus B: Chemical and Physical Meteorology* **61**, 51–63 (2009).

1122 102. Fratini, G., Ciccioli, P., Febo, A., Forgione, A. & Valentini, R. Size-segregated
1123 fluxes of mineral dust from a desert area of northern China by eddy covariance.
1124 *Atmospheric Chemistry and Physics* **7**, 2839–2854 (2007).

1125 103. Miller, R. L. et al. Mineral dust aerosols in the NASA Goddard Institute for Space
1126 Sciences ModelE atmospheric general circulation model. *Journal of Geophysical*
1127 *Research* **111**, D06208 (2006).

1128 104. Hurrell, J. W. et al. The Community Earth System Model: A Framework for
1129 Collaborative Research. *Bulletin of the American Meteorological Society* **94**, 1339–
1130 1360 (2013).

1131 105. Michou, M., Nabat, P. & Saint-Martin, D. Development and basic evaluation of a
1132 prognostic aerosol scheme (v1) in the CNRM Climate Model CNRM-CM6.
1133 *Geoscientific Model Development* **8**, 501–531 (2015).

1134 106. Ito, A. & Kok, J. F. Do dust emissions from sparsely vegetated regions dominate
1135 atmospheric iron supply to the Southern Ocean? *Journal of Geophysical Research: Atmospheres* **122**, 3987–4002 (2017).

1137 107. Schmid, B. et al. Evaluation of the applicability of solar and lamp radiometric
1138 calibrations of a precision sun photometer operating between 300 and 1025 nm.
1139 *Applied Optics* **37**, 3923 (1998).

1140 108. Giles, D. M. et al. Advancements in the Aerosol Robotic Network (AERONET)
1141 Version 3 database – automated near-real-time quality control algorithm with

1142 improved cloud screening for Sun photometer aerosol optical depth (AOD)
1143 measurements. *Atmospheric Measurement Techniques* **12**, 169–209 (2019).

1144 109. Kim, D. et al. Dust optical properties over North Africa and Arabian Peninsula
1145 derived from the AERONET dataset. *Atmospheric Chemistry and Physics* **11**,
1146 10733–10741 (2011).

1147 110. Russell, P. B. et al. A multiparameter aerosol classification method and its
1148 application to retrievals from spaceborne polarimetry. *Journal of Geophysical
1149 Research: Atmospheres* **119**, 9838–9863 (2014).

1150 111. Dubovik, O. et al. Variability of Absorption and Optical Properties of Key Aerosol
1151 Types Observed in Worldwide Locations. *Journal of the Atmospheric Sciences* **59**,
1152 590–608 (2002).

1153 112. Randles, C. A. et al. The MERRA-2 Aerosol Reanalysis, 1980 Onward. Part I:
1154 System Description and Data Assimilation Evaluation. *Journal of Climate* **30**, 6823–
1155 6850 (2017).

1156 113. Weinzierl, B. et al. The Saharan Aerosol Long-Range Transport and Aerosol–
1157 Cloud-Interaction Experiment: Overview and Selected Highlights. *Bulletin of the
1158 American Meteorological Society* **98**, 1427–1451 (2017).

1159 114. Weinzierl, B. et al. Airborne measurements of dust layer properties, particle size
1160 distribution and mixing state of Saharan dust during SAMUM 2006. *Tellus B: Chemical and Physical Meteorology* **61**, 96–117 (2009).

1162 115. Gliß, J. et al. AeroCom phase III multi-model evaluation of the aerosol life cycle
1163 and optical properties using ground- And space-based remote sensing as well as
1164 surface in situ observations. *Atmospheric Chemistry and Physics* **21**, 87–128
1165 (2021).

1166 116. Liu, D. et al. Aircraft and ground measurements of dust aerosols over the west
1167 African coast in summer 2015 during ICE-D and AER-D. *Atmospheric Chemistry and Physics* **18**, 3817–3838 (2018).

1168 117. Denjean, C. et al. Size distribution and optical properties of mineral dust aerosols
1169 transported in the western Mediterranean. *Atmospheric Chemistry and Physics* **16**,
1170 1081–1104 (2016).

1172 118. Adebiyi, A. A. et al. Dust Constraints from joint Observational-Modelling-
1173 experiMental analysis – DustCOMM Version 1. Zenodo [Data set]-[Data set]
1174 (2019) doi:10.5281/zenodo.2620475.

1175 119. Adebiyi, A. First release of DustCOMM. Zenodo [Code]-[Code] (2019)
1176 doi:10.5281/ZENODO.2620556.

1177 120. Adebiyi, A. A. et al. DustCOMM_v1 Input Dataset. Zenodo **[Data set]**, (2019).

1178 121. Adebiyi, A., Huang, Y. & Samset, B. Adebiyi et al: absorption of shortwave
1179 radiation by North African dust. (2022) doi:10.5281/zenodo.6406831.

1180 122. Adebiyi, A. A. & Kok, J. F. Climate models miss most of the coarse dust in the
1181 atmosphere. *Science Advances* **6**, eaaz9507 (2020).

1182
1183

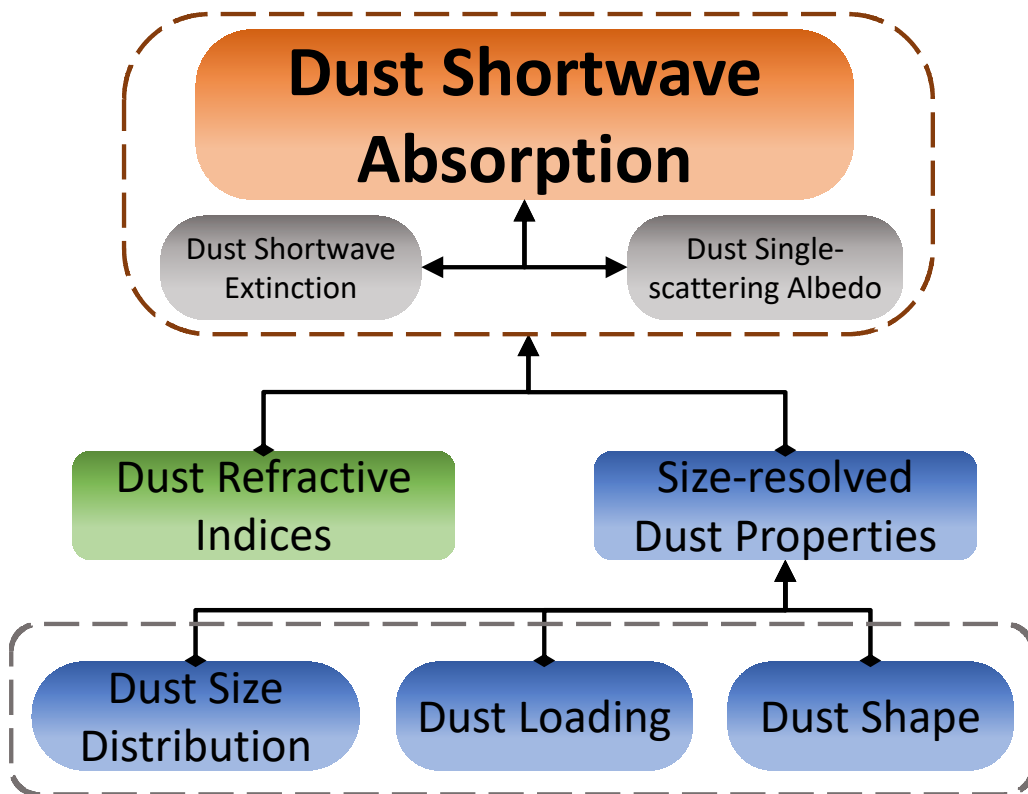


Figure 1: **Dust shortwave absorption depends on dust microphysical properties.** Dust shortwave absorption – quantified by the dust absorption aerosol optical depth (dust AAOD) – depends on dust shortwave extinction and dust single scattering albedo, both of which depend on dust microphysical properties. Direct and continuous observations of these microphysical properties, including, dust refractive index, dust size distribution, and dust shape, are difficult to obtain from remote-sensing platforms. Therefore, overall uncertainties in dust shortwave absorption depend primarily on the uncertainties in these microphysical properties. To obtain constraints on dust AAOD at 550 nm wavelength, we obtained constraints on dust refractive index in this study, which leveraged over a dozen measurements of dust single-scattering albedo at 550 nm wavelength over North Africa (green shaded box; see Methods). These constraints are then combined with observationally informed constraints on dust size distribution, dust loading, and dust shape from previously-published datasets that similarly leveraged in-situ measurements of dust properties (blue shaded boxes)^{3,21,27,93} to obtain constraints on dust AAOD.

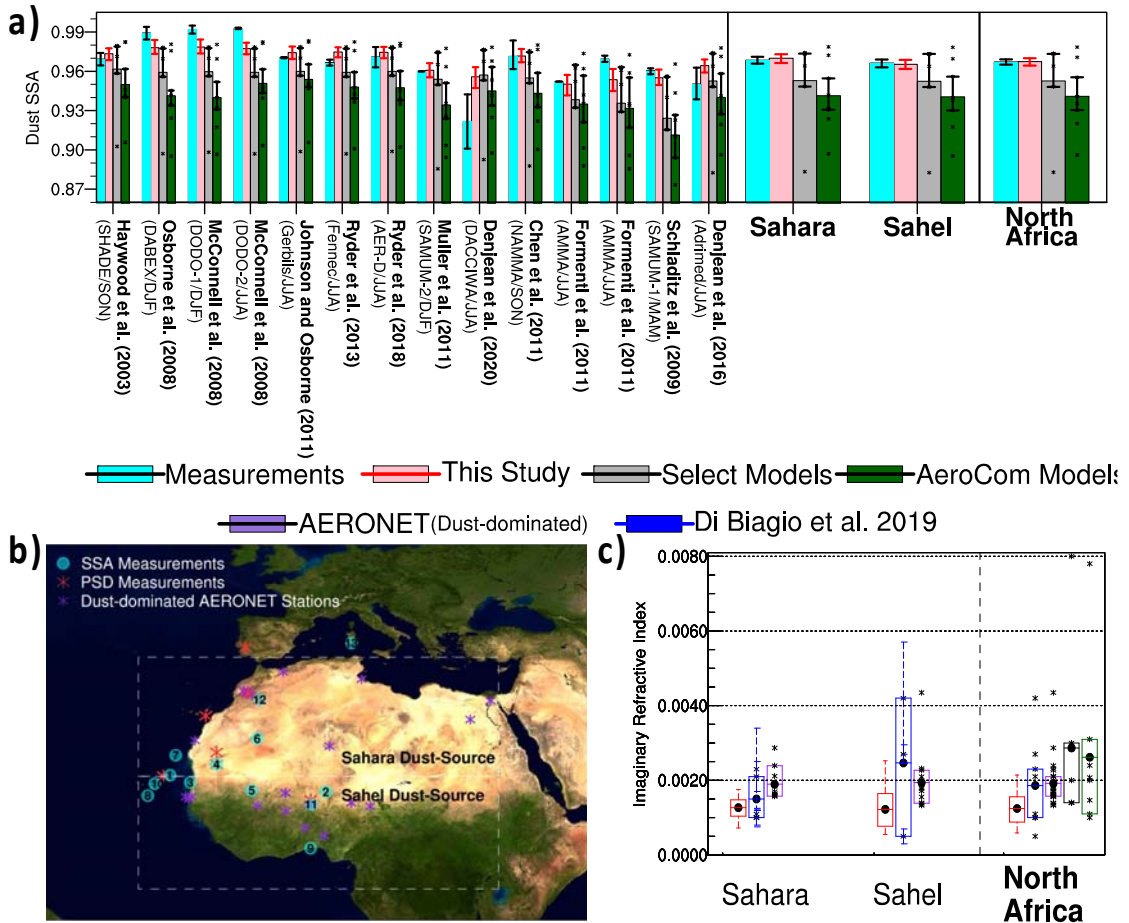
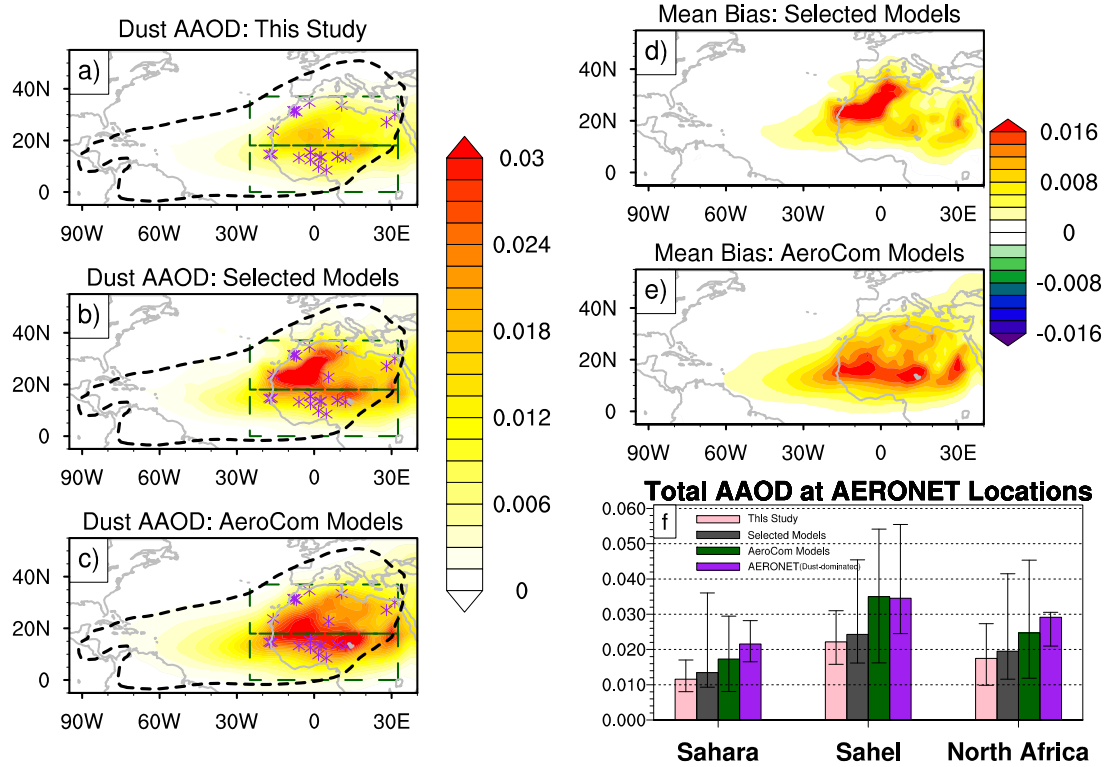


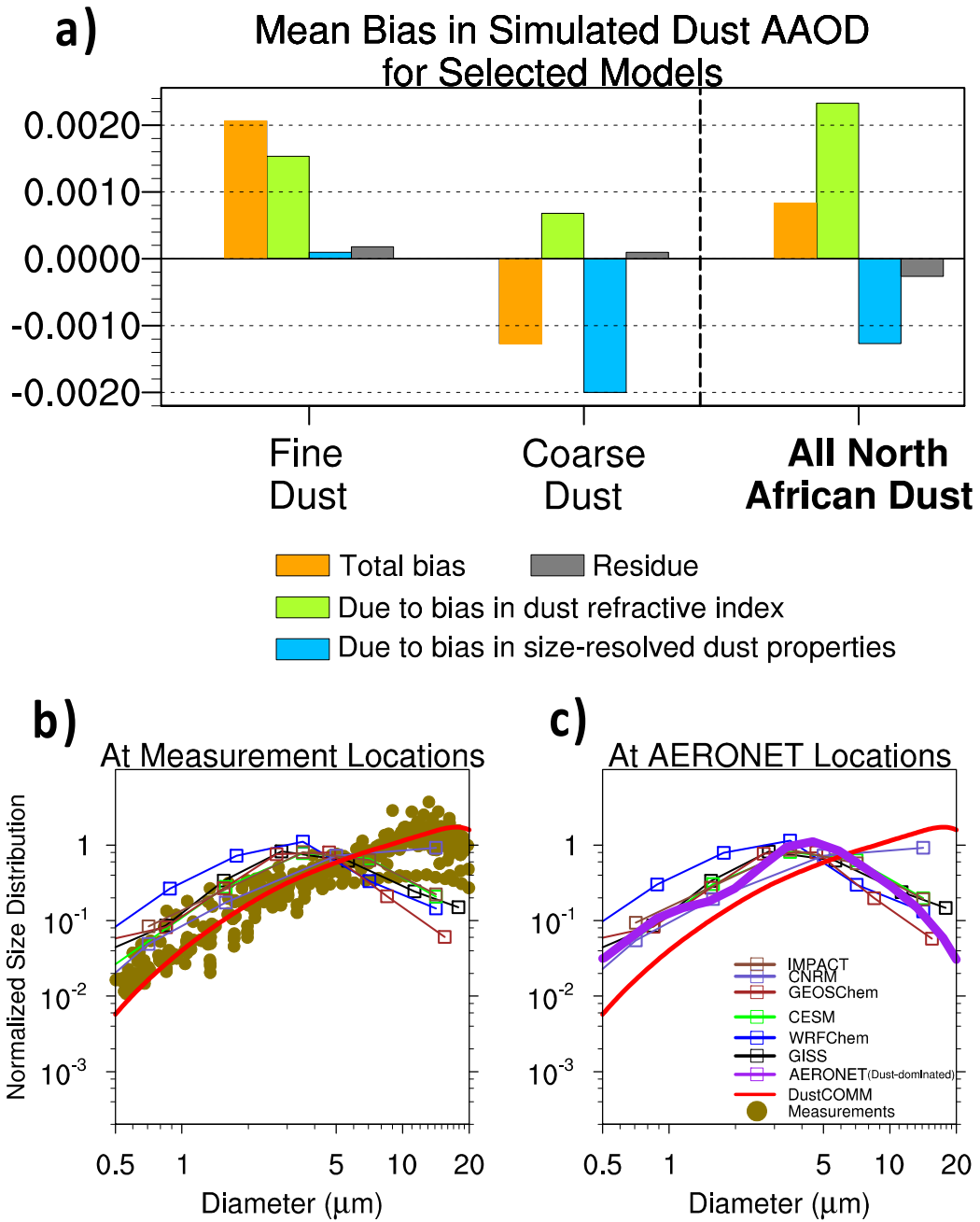
Figure 2: **Climate and chemical transport models underestimate dust single-scattering albedo and overestimate dust imaginary refractive index over North Africa.** (a) The dust single-scattering albedo (SSA) at 550 nm wavelength obtained from in-situ measurements over North Africa (cyan bars) and the corresponding estimates from this study (pink/red bars), from an ensemble of six selected global aerosol models (gray bars), and from an ensemble of eight AeroCom Phase III models (dark green bars; Aerosol Comparison between Observations and Models project). Details of the models that are part of the selected and AeroCom model ensembles are provided in Methods and Table S-2. The figure also includes the regionally averaged SSA at 550 nm wavelength for the Sahara and Sahel regions and for all of North Africa, as defined by the dashed boxes in Figure 2b. The black/red vertical lines on the bars indicate the one standard error range, and the black dots represent the values from individual models in the two ensembles. (b) The locations of the 14 dust SSA in-situ measurements (cyan circles), 12 dust size distribution measurements (obtained from Adebiyi et al.¹²², red stars), and 23 dust-dominated AERONET stations (purple stars; see Methods) that are used as part of this study. Details of the in-situ dust SSA measurements can be found in Table S-1 and section S-1. The boxes in (b) delineate the Sahara (25W-32.5E; 18-37N) and Sahel (25W-32.5E; 0-18N) dust source regions. (c) Comparison between the constraints on the dust imaginary refractive index at 550-nm wavelength obtained from this study (red/pink), from laboratory measurements of dust generated from several North African soil samples by Di Biagio et al.²⁹ (blue), and from AERONET dust-dominated observations (purple),

1223 both interpolated to 550 nm over the Sahara and Sahel regions (see Method for details).
1224 The figure also includes spatially invariant imaginary refractive index values used in an
1225 ensemble of selected global aerosol models (gray) and an ensemble of AeroCom models
1226 (dark green) at 550 nm wavelength. The box boundaries approximately indicate one
1227 standard error range; the horizontal lines and solid dots within the box denote the mean
1228 values; the red vertical lines indicate the 95% confidence interval. Finally, the stars
1229 represent the member values used in the calculation.

1230



this study, (b) an ensemble of six selected models, and (c) an ensemble of eight AeroCom models. (d) & (e) The corresponding mean bias in the ensemble of selected and AeroCom models, respectively, relative to our constraints on dust AAOD. Dashed black lines in Figure 3a-c delineates the region where dust emitted from North African dust sources account for more than 80 % of annual dust loading⁵⁰, and the dashed green boxes delineate the Sahara and Sahel regions shown in Figure 2b. (f) Total AAOD (dust plus non-dust AAOD) estimated at dust-dominated AERONET stations (purple stars in Figure 3a-c), for this study (pink bars), an ensemble of selected models (dark-grey bars), an ensemble of AeroCom models (dark-green bars), and AERONET retrievals (purple bars). The total AAOD for this study and the ensemble of selected models includes the ensemble of non-dust AAOD obtained from the AeroCom models. The AERONET total AAOD minimizes the non-dust components in the resulting estimates by applying several criteria (see Methods for details). The black vertical lines on the bars denote one standard error range.



1248

1249 *Figure 4: The decomposition of the bias in the simulated dust aerosol absorption*
1250 *optical depth. (a) Averaged over the region where North African dust sources dominate*
1251 *global dust loading (by more than 80 %; see dashed contour in Figure 3)⁵⁰, the mean*
1252 *bias in simulated dust aerosol absorption optical depth (dust AAOD), including the total*
1253 *mean bias (orange bar) and the bias due to dust refractive index (green-yellow bar) and*
1254 *size-resolved dust properties (blue bar) which includes the biases in dust load, dust*
1255 *shape, and dust size distribution, obtained for the ensemble of six global aerosols models,*
1256 *and averaged for fine dust (diameter, $D \leq 5 \mu\text{m}$), coarse dust ($D \geq 5 \mu\text{m}$), and all dust of*
1257 *North African origin. The residue (grey bar) is the difference in the total bias in dust*

1258 *AAOD and the sum of the bias due to the bias in refractive index and size-resolved dust*
1259 *properties. (b & c) The normalized dust size distributions obtained from in-situ*
1260 *measurements (dark gold dots), collocated DustCOMM constraints on dust size*
1261 *distribution (red), and collocated estimates from six selected global aerosol model*
1262 *simulations (see Table S-1) and the aerosol size distribution obtained from AERONET*
1263 *retrievals (purple), compared at the locations of (b) the in-situ measurements and (c) the*
1264 *dust-dominated stations (see Figure 2b) over North Africa. All size distributions are*
1265 *normalized between 2.5 and 10 μm (see Methods).*

1266
1267

Dust Shortwave

Absorption

Dust Shortwave
Extinction

Dust Single-
scattering Albedo

Dust Refractive
Indices

Size-resolved
Dust Properties

Dust Size
Distribution

Dust Loading

Dust Shape

